Spatiotemporal Characteristics of Atmospheric NO_2 Concentration in Southeast Asia using Satellite Observations

Piromthong, P.,[1] Satirapod, C.,[1] Trivitayanurak, W.[2] and Weerawong, K.[1*]
[1]Mapping and Positioning from Space (MAPS) Technology Research Center, Department of Survey Engineering, Faculty of Engineering, Chulalongkorn University, Thailand
E-mail: pawan.p@chula.ac.th, chalermchon.s@chula.ac.th, kanok.w@chula.ac.th
[2]Department of Environmental and Sustainable Engineering, Faculty of Engineering, Chulalongkorn University, Thailand, E-mail: win.t@chula.ac.th
Corresponding Author

DOI: https://doi.org/10.52939/ijg.v22i7.5080

Abstract
Southeast Asia has long experienced severe air pollution, posing significant risks to public health. Contrary to global trends of declining emissions, the region's rapid industrialization may exacerbate air quality problems. This study investigates the spatiotemporal characteristics of atmospheric nitrogen dioxide (NO_2) concentrations across Southeast Asia using satellite-based observations. Two analytical approaches are employed: an analysis of tropospheric NO_2 concentration fields and a flux-divergence-based assessment of NO_2 emissions. First, regional and local patterns of NO_2 concentrations are examined using tropospheric column density data from the Ozone Monitoring Instrument (OMI) for the period 2005–2022. The results indicate that elevated NO_2 concentrations are primarily concentrated in major urban centers, likely associated with vehicular emissions and industrial activities. Notably, enhanced NO_2 levels are also observed in several forested regions. These anomalies are hypothesized to be associated with biomass burning, a relationship further supported through integration with MODIS burned area products. Detailed analyses are then conducted for 12 hotspot regions using time series decomposition to isolate long-term trends, seasonal variability, and residual components. To account for the potential influence of the COVID-19 pandemic, the analysis period for each hotspot is divided into pre- and post-pandemic phases, revealing distinct concentration trends for individual regions. Second, NO_2 emission patterns are investigated using flux divergence calculations derived from TROPOspheric Monitoring Instrument (TROPOMI) observations in combination with wind fields from the ECMWF ERA5 reanalysis. Regional-scale emission maps are first produced for Southeast Asia, followed by focused analyses for three selected areas: the Bangkok Metropolitan Region, the Northern Vietnam Industrial Corridor, and the Singapore–Kuala Lumpur Region. Independent auxiliary datasets are used to reference the accuracy of the inferred emission patterns. The results demonstrate that the flux divergence approach effectively identifies major emission sources, especially in complex areas like Bangkok's urban region.

Keywords: Flux Divergence, Nitrogen Dioxide, OMI, Southeast Asia, Time-Series Analysis, TROPOMI

1. Introduction

Air pollution remains a major global environmental issue, posing substantial risks to human health, ecological systems, and socioeconomic sustainability. Among the major atmospheric trace gases, nitrogen dioxide (NO_2) is of particular concern due to its strong links to adverse respiratory outcomes, including bronchitis, reduced lung development in children [1], elevated lung cancer risk [2], and elevated mortality rates [3]. Beyond its direct toxic effects, NO_2 plays a crucial role in atmospheric chemistry by contributing to the formation of secondary inorganic aerosols especially nitrate particles which constitute a large fraction of fine particulate matter (PM2.5). Furthermore, nitrogen oxides ($NO_x = NO + NO_2$) [4] are key precursors in photochemical reactions that produce tropospheric ozone (O_3), a pollutant that harms respiratory health [1] and indirectly cause harm through photochemical smog and acid rain. Given these multifaceted impacts, understanding the sources, dynamics, and spatial variability of NO_2 is critical for effective air quality management.

NO_2 emissions originate from both anthropogenic (65%) and natural (35%) sources [5]. Anthropogenic NO_2 is mainly emitted through fossil fuel combustion associated with transportation, power generation, and industrial activities, resulting in elevated concentrations in densely populated and industrialized regions. These emissions are influenced by socioeconomic factors such as settlement density and income levels [6]. Temporal variations in traffic and industrial activity further contribute to fluctuations in NO_2 levels [7]. Natural sources of NO_2 include forest fires, lightning, and microbial activity in soils. Unlike anthropogenic sources, which are relatively stable, natural emissions are more complex and variable in space and time. Understanding these variations is essential for designing effective mitigation strategies, which may include industrial emission controls, the promotion of electric vehicles, and early warning systems for natural emission events such as seasonal forest fires.

Globally, average NO_2 emissions have declined over the past century [8], particularly in high-income countries such as China [9], the United States [10] and [11], and across Europe [12], largely due to the implementation of stringent environmental regulations [9][13][14] and [15]. In contrast, several developing regions continue to experience stable or increasing NO_2 levels due to rapid urbanization, industrial expansion, and comparatively limited regulatory enforcement. This study focuses on mainland Southeast Asia, encompassing Cambodia, Laos, Malaysia, Myanmar, Singapore, Thailand, and Vietnam (Figure 1). Except for Singapore, these countries are classified as middle-income and are developing their economies. Between 2010 and 2019, their GDP grew by 6%, surpassing the average growth rates of low-, middle-, and high-income countries (2.1%, 5.3%, and 2.1%, respectively) [16]. Since 2018, foreign direct investment growth in Southeast Asia has exceeded 10% annually, with the manufacturing sector accounting for nearly one-quarter of total inflows [17], contributing to increased industrial activity and vehicular traffic.

The public health implications of deteriorating air quality in Southeast Asia are substantial. According to the World Health Organization (WHO), ambient air pollution was responsible for over 3 million deaths in 2012 and 4.2 million premature deaths in 2019 [6] and [18], with approximately 89% of these occurring in low- and middle-income countries. In Southeast Asia, premature deaths from air pollution were 2.95% and 3.30% of the total in 2012 and 2019, respectively [19]. While the global average increased by 40%, Southeast Asia experienced a 56.5% rise. Notably, Singapore, Vietnam, and Malaysia experienced increases of 81.3%, 92.3%, and 168.5%, respectively. In Myanmar and Thailand, over 20,000 annual deaths are linked to air pollution, likely exacerbated by recurring forest fires [20]. Cambodia, Laos, Thailand, and Myanmar frequently experience fires during the dry season (February to April), often associated with slash-and-burn agricultural practices [21][22] and [23]. Myanmar, in particular, exhibits one of the highest fire occurrence rates in South and Southeast Asia [24]. This underscores the complex interaction between natural emission sources, anthropogenic activities, and regional air quality.

While in-situ air quality monitoring provides accurate ground-level NO_2 measurements, it is constrained by high operational costs and sparse spatial coverage, limiting its applicability for comprehensive regional-scale assessments, given the spatial heterogeneity of NO_2 emissions. Satellite remote sensing offers an effective alternative by providing spatially continuous, temporally consistent observations over large areas. Atmospheric NO_2 has been monitored from space for more than two decades. The Global Ozone Monitoring Experiment (GOME) [25], operated from 1995 to 2011, followed by the SCanning Imaging Absorption spectroMeter for Atmospheric ChartographY (SCIAMACHY) [26] collected data from 2002 to 2012. The Ozone Monitoring Instrument (OMI), Global Ozone Monitoring Experiment 2 (GOME-2) [27], and TROPOspheric Monitoring Instrument (TROPOMI), have been collecting data since 2005, 2006, and 2017, respectively, and are still operational. Among these, the OMI and TROPOMI datasets used in this study offer relatively high spatial resolution and daily global coverage, making them particularly valuable for both temporal and spatial analyses.

OMI has provided a continuous record of tropospheric NO_2 observations since 2005, enabling robust assessments of long-term trends and interannual variability, while TROPOMI provides the highest spatial resolution currently available, enabling detailed spatial assessments. These datasets have been widely used to study atmospheric NO_2 across various regions, including global studies [8][28] and [29], as well as research focused on Europe [30][31][32] and [33], Asia [34][35][36] and [37], and particularly China [9][38][39] and [40]. However, comprehensive investigations integrating long-term and high-resolution satellite data to examine NO_2 dynamics in Southeast Asia remain limited.

To address this gap, this study investigates the temporal characteristics of NO_2 concentrations in Southeast Asia using 18 years of OMI observations, with time series decomposition applied to major emission hotspots. Furthermore, high-resolution

TROPOMI data combined with flux divergence analysis are employed to examine the spatial distribution of NO_2 emissions. By integrating satellite observations with spatial analysis techniques, this study aims to provide a comprehensive assessment of NO_2 variability and to support regional air quality management from a geoinformatics perspective.

2. Data

This study integrates multiple satellite and reanalysis datasets to support a dual analytical framework for characterizing NO_2 concentrations and estimating emissions over Southeast Asia. Among the various satellite instruments used to monitor atmospheric NO_2, OMI and TROPOMI provide relatively high spatial resolution and near-daily global coverage. In particular, OMI has been continuously operating since 2005, offering a long-term dataset suitable for analysing temporal variability, while TROPOMI provides much finer spatial resolution for resolving detailed spatial patterns and supporting flux divergence analysis for emission mapping. Given the significant influence of biomass burning on air quality in Southeast Asia, fire activity is characterized using the MODIS Burned Area product, which combines spectral change detection and fire hotspot information to provide robust estimates of burned areas at 1 km resolution. Meteorological data, specifically horizontal wind fields, are obtained from the ERA5 reanalysis produced by ECMWF, which is widely regarded as one of the most reliable global datasets and is essential for deriving the flux divergence calculations. These datasets are selected due to their complementary strengths in temporal coverage and spatial resolution, as well as their extensive validation and widespread use in atmospheric researchs. Together, they provide a coherent framework for analysing both the temporal evolution and spatial distribution of NO_2 over the study region.

2.1 Ozone Monitoring Instrument (OMI) Data

OMI consists of two imaging grating spectrometers operating in the visible and ultraviolet spectrum of the wavelengths (270–500 nm) with the normal spatial resolution of 13 × 24 km² at nadir to 24 × 160 km² at the swath periphery [41]. It was launched in July 2004 aboard the NASA Aura satellite orbiting the earth at an altitude of 705 km in a sun-synchronous polar orbit with a daily equatorial crossing at approximately 13:30–13:45 local time on the ascending node. Operating at an orbital inclination of 98.1°, the instrument achieves a latitudinal coverage spanning from 82° N to 82° S. As a wide-field-imaging spectrometer with a 114° across-track field of view, it generates a 2,600 km swath.

One of the primary objectives of OMI is to measure trace gases including nitrogen dioxide. Atmospheric NO_2 concentrations are retrieved by the OMI through the analysis of backscattered solar radiation. The retrieval process primarily utilizes the distinct absorption features within the visible spectrum (approx. 405–465 nm). By applying the Differential Optical Absorption Spectroscopy (DOAS) technique, broadband attenuation is filtered from the measured radiance. The remaining high-frequency absorption signatures are fitted to laboratory-measured cross-sections to determine the Slant Column Density (SCD), which represents the total integrated concentration along the effective optical path. To obtain the Vertical Column Density (VCD), the SCD is normalized using an Air Mass Factor (AMF). This factor incorporates critical parameters including observation geometry, surface reflectivity, cloud conditions, and the vertical distribution of NO_2 derived from chemical transport models, typically the TM4 model for OMI retrievals [42]. The total VCD is subsequently partitioned into stratospheric and tropospheric components via model-based spatial filtering. The resulting tropospheric column serves as a primary proxy for boundary-layer pollution. Retrieval precision is fundamentally constrained by uncertainties associated with the AMF, cloud interference, and the assumed vertical distribution of the NO_2.

The OMI Level 3 (OMI L3) products, used in this study, resample the NO_2 concentrations data into a 0.25° × 0.25° latitude–longitude grid. The OMI L3 daily product is provided as a single file, consolidating 14-15 swath data collected by OMI in a single day, resulting in overlapping fields of view and pixel spans in some grids. The weighted average of binned pixels in each grid is calculated using inverse proportional grid size and proportional area of overlap. The OMI L3 products are available online (https://disc.gsfc.nasa.gov/datasets/OMNO2d_003/summary) and provided in molecules/cm² units. Additionally, this includes estimates of tropospheric NO_2 vertical column density, following the methodology of [43].

Due to high humidity and persistent cloud cover in Southeast Asia, daily OMI data often contain a significant number of unreliable pixels. Therefore, monthly average gridded NO_2 values are employed in this study instead of daily data. The monthly mean data for the OMI L3 product are calculated using a weighted average. This method employs the Weight parameter from the downloaded files, which represents the total weights of all NO_2 OMI measurements recorded during the creation of the

ISSN: 1686-6576 (Printed) | ISSN 2673-0014 (Online) | © Geoinformatics International

daily file, on a 0.25° x 0.25° latitude-longitude grid [44].

2.2 TROPOspheric Monitoring Instrument (TROPOMI) Data

TROPOMI is a high-resolution imaging spectrometer onboard the European Space Agency's Sentinel-5 Precursor (S5P) satellite, launched in 2017, as part of the Copernicus Programme targeted to monitoring air pollution. The satellite operates in a polar, Sun-synchronous orbit at the altitude of 824 km with a Local Time of Ascending Node of 13:30 hours. TROPOMI collects data every second with a swath width of 2,600 km. Its spatial resolution at nadir was 7 × 3.5 km² prior to August 6, 2019, and improved to 5.5 × 3.5 km² thereafter. TROPOMI uses a similar data acquisition approach compared to OMI but with better spatial resolution and signal quality [45]. It measures backscattered solar radiation in ultraviolet, visible, near and short-wavelength infrared bands which can be employed to monitor ozone, methane, formaldehyde, aerosol, carbon monoxide, sulphur dioxide and nitrogen dioxide in the atmosphere [46]. The algorithm used to retrieve atmospheric NO2 is similar to that of OMI as described previously. In this study, the TROPOMI Level-2 (TROPOMI L2) NO_2 product will be used in the process of flux computation.

2.3 MODIS Burned Area Product

The Moderate Resolution Imaging Spectroradiometer (MODIS) instruments were launched aboard the Terra and Aqua satellites in 1999 and 2002, respectively, and have included capabilities for global fire monitoring. The MODIS Burned Area product [47] is a dataset derived from MODIS observations and generated using a dedicated burned area mapping algorithm that integrates spectral information with MODIS active fire detections. In this study, we use the latest Collection 6 version of the MODIS Burned Area product, which provides per-pixel information on burned area extent and associated data quality at a spatial resolution of 500 m. Burned areas are characterized by persistent surface alterations, including ash and charcoal deposition, loss of vegetative cover, and changes in the physical structure of the land surface. The MODIS Burned Area algorithm identifies such areas by tracking spectral, temporal, and structural changes consistent with fire-affected surfaces, enabling the detection of both the spatial extent and approximate timing of burning events. Unlike the MODIS Active Fire product [48], which provides instantaneous detections of thermal anomalies at the time of satellite overpass, the MODIS Burned Area product employs multi-temporal post-processing that integrates reflectance changes, temporal persistence, and active fire information to map cumulative fire-affected areas. This characteristic makes the product particularly suitable for investigating historical fire activity and assessing the relationship between biomass burning and atmospheric NO_2 variability, especially in regions such as Southeast Asia where fires may be intermittent or partially obscured by cloud cover.

2.4 European Centre for Medium-Range Weather Forecasts (ECMWF) Reanalysis v5 (ERA5) Data

The European Centre for Medium-Range Weather Forecasts (ECMWF) Reanalysis v5 (ERA5) provides a comprehensive global atmospheric reanalysis dataset spanning from 1940 to the present. ERA5 combines numerical weather prediction model output with a wide range of satellite and in-situ observations using advanced data assimilation techniques, producing spatially and temporally consistent representations of atmospheric, land surface, and oceanic variables. Among these variables, ERA5 provides hourly wind fields at multiple pressure levels, which are widely used in atmospheric transport, dispersion, and emission studies.

In this study, wind data at the 1000 hPa pressure level are used to represent near-surface atmospheric conditions for flux divergence analysis of NO_2 emissions. Although ERA5 also provides 10 m wind data, winds at the 1000 hPa level are preferred because they are less directly affected by local surface roughness, land-cover heterogeneity, and parameterization of surface-layer processes, which can introduce additional uncertainties, particularly in regions with complex terrain and rapidly changing land use. As a result, 1000 hPa winds are commonly adopted in regional-scale atmospheric transport and emission analyses as a more stable proxy for near-surface flow patterns influencing pollutant dispersion.

However, it should be noted that there is an inherent limitation regarding the vertical representativeness of the wind field used in the flux divergence calculation. The TROPOMI tropospheric NO_2 VCD is a column-integrated quantity and therefore includes contributions from multiple altitude levels without explicitly preserving the vertical distribution of NO_2. Nevertheless, the use of near-surface wind fields (e.g., ERA5 at 1000 hPa) can be justified based on well-established atmospheric boundary layer (PBL) theory. Most anthropogenic NO_2 emissions originate near the surface and are largely confined within the PBL, which typically extends to about 1 km [49]. Due to strong vertical gradients in wind speed and

ISSN: 1686-6576 (Printed) | ISSN 2673-0014 (Online) | © Geoinformatics International

atmospheric stability between the PBL and the free troposphere, vertical exchange is often limited, and the majority of NO_2 remains within this layer. As a result, although the VCD is column-integrated, its dominant variability over polluted regions is primarily driven by near-surface processes within the PBL, supporting the use of a representative wind field from this layer as a proxy for transport.

We acknowledge that selecting an optimal representative wind height is not straightforward, as wind characteristics vary with altitude. However, previous studies indicate that the flux divergence method is relatively insensitive to the choice of wind representation within the PBL. For example, [32] found only minor differences between single-level and vertically averaged winds, while [50] reported emission variations of approximately 10% across different altitudes. Subsequent studies using lower representative heights (e.g., 300 m [51]) and 100 m [37] have similarly shown consistent results, further supporting the robustness of the method. Therefore, adopting a single representative wind level, such as ERA5 winds at 1000 hPa, provides a practical approach for mapping emission patterns. As the primary objective of this study is to characterize spatial distributions rather than derive highly precise emission magnitudes, any systematic bias introduced by the choice of wind height is expected to have a limited impact on the main conclusions. To align with the overpass time of the Sentinel-5P satellite (approximately 13:30–13:45 local time), hourly ERA5 wind fields are linearly interpolated between 13:00 and 14:00 local time. The original wind data, provided at a spatial resolution of 0.25° × 0.25°, are further interpolated to the 2 km grid used for the NO_2 dataset to ensure spatial consistency between meteorological fields and satellite-derived atmospheric observations.

As with all reanalysis products, ERA5 wind fields are subject to uncertainties related to model physics, data assimilation, and spatial resolution, which may be larger near the surface and in data-sparse regions such as parts of Southeast Asia. Nevertheless, ERA5 has been widely evaluated and extensively used in atmospheric and air quality studies, owing to its consistency, high temporal resolution, and free and open accessibility, making it suitable for regional-scale flux divergence and atmospheric transport analyses.

3. Investigation Based on Temporal Characteristics

3.1 Methodology

The OMI L3 products are used to investigate the temporal characteristics of atmospheric NO_2 concentrations across Southeast Asia due to its long-term data record. However, given the frequent cloud cover in the region, temporal averaging is essential for robust analysis. To identify long-term trends and seasonal variations across key emission hotspots, monthly averages are computed based on the OMI L3 data from 2005 to 2022. The averages are used to plot concentrations maps and in time series decomposition. The NO_2 concentrations over a period of time, denoted as c, can be decomposed into three components: the long-term trend (T), seasonal variation (S), and residual noise (N), as defined in Equation 1:

$$c = T + S + N$$

Equation 1

Initially, pixels representing NO_2 concentration for each area of the hotspots are selected. Given the significant disruption to human activity caused by the COVID-19 pandemic, the dataset is divided into two periods: pre-pandemic (September 2005–December 2019) and post-pandemic (April 2020–December 2022). Linear, quadratic, and cubic models are fitted to the trend data to capture different temporal variations. To extract the seasonal component, the data are detrended by subtracting the estimated trend from the original time series. Monthly medians are then computed to represent typical seasonal behaviour, with the medians preferred over the means to reduce the influence of outliers. This decomposition method allows for any seasonal pattern and does not require prior knowledge of a mathematical function or residual component (N) which represents noise and anomalies and is calculated as the difference between the observed data and the sum of the trend and seasonal components. Although this study does not specifically investigate this noise component, it does offer the opportunity to identify unusual occurrences more systematically.

3.2 Results and Discussion

3.2.1 Overall analysis

A simple map of Southeast Asia is shown in Figure 1(a), including major hotspot areas such as Bangkok (BKK), Chiang Mai (CNX), Mea Moh Mine (MMM), Kuala Lumpur (KUL), Singapore (SIN), Ho Chi Minh (HCM), Hanoi (HAN), Haiphong (HIP), Phanom Pehn (PNP), Vientiane (VIT), Nay Pyi Taw (NPT), and Mandalay (MDL). Two rectangles indicate example areas along the Thailand-Cambodia (A) and Thailand-Myanmar (B) borders where forest fires occur annually, which will be investigated later.

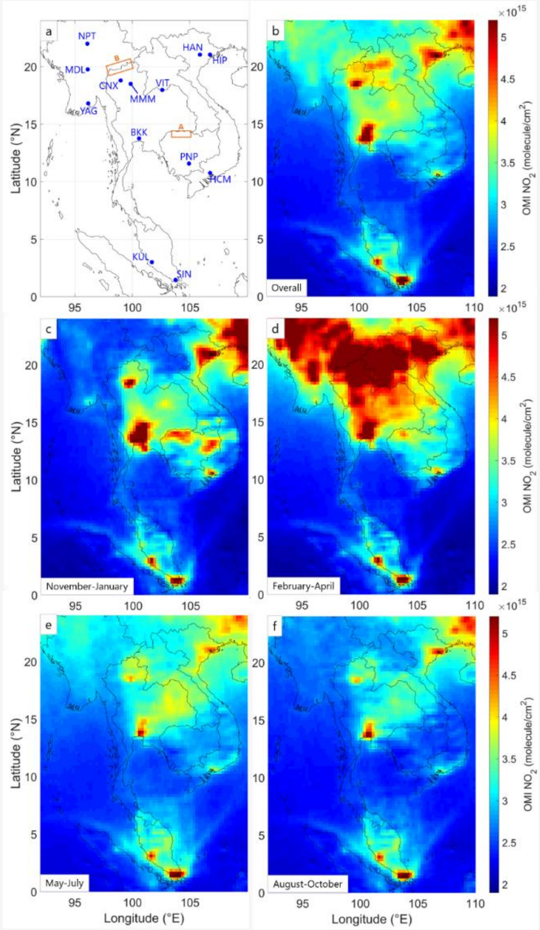

Figure 1: (a) Study areas including hotspot areas such as Bangkok (BKK), Chiang Mai (CNX), etc. and two example areas represented by rectangle A (along the Thailand-Cambodia border) and rectangle B (along the Thailand-Myanmar border). (b) Mean NO_2 concentrations over the study period. (c-f) Mean NO_2 concentrations from December-January, February-April, May-July, and August-November, respectively.

Figure 1(b) illustrates the mean NO_2 concentrations over the study period, highlighting elevated levels in major urban and industrial centers such as Singapore, Kuala Lumpur, Ho Chi Minh City, Hanoi, Bangkok, and the Mae Moh power plant in northern Thailand. These elevated concentrations are primarily attributed to fossil fuel combustion from transportation and industrial activities. Additionally, widespread NO_2 concentrations are observed across northern Thailand, Laos, and Myanmar, suggesting contributions from both anthropogenic and biomass burning sources, despite the averaging values not clearly highlighting them. This section reveals that NO_2 concentrations in Southeast Asia are influenced by both anthropogenic sources and forest fires, contributing to the widespread NO_2 in northern Thailand, Laos, and Myanmar.

To characterize seasonal patterns, we divide the year into four three-month intervals. The first period, November to January (Figure 1(c)), corresponds to the coolest season, with average minimum temperatures ranging from 26°C in Singapore to 15°C in northern Laos. NO_2 concentrations in the hotspots, including major cities and the Mae Moh mine, peak during this period. This seasonal increase is consistent with the longer atmospheric lifetime of NO_2 under cooler conditions, allowing for accumulation and then resulting in higher concentrations compared to other times of the year. Notably, elevated NO_2 levels are also detected in non-urban areas of Cambodia, specifically in the area marked as rectangle A in Figure 1(a), where no major anthropogenic sources are present. These concentrations are linked to biomass burning. To investigate this, we utilize the MODIS Burned Area product to display spatial correlations between areas with high NO_2 levels and burned areas. We specifically use the 18-year GeoTiff MCD64 monthly Burn Date product developed by the University of Maryland, which provides monthly burned areas in a geographic latitude-longitude grid format.

Figure 2 presents monthly comparisons of NO_2 concentrations and burned areas for 2007. These comparisons reveal a consistent spatial overlap between high NO_2 concentrations and burned areas in the region every year from January to December for 18 years (2005-2022). The northern boundary of these burned areas aligns with the Thailand-Cambodia border, where topographic elevation increases by approximately 300 meters. This elevation transition appears to act as a barrier, limiting the spread of fires and associated NO_2 emissions into Thailand. The abrupt spatial cutoff in NO_2 concentrations at this boundary suggests that fire-related NO_2 is predominantly confined below 300 meters in altitude. The most severe fire-related pollution occurs between February and April, the hottest and driest season in Southeast Asia (Figure 1(d)). During this period, widespread NO_2 pollution is observed across northern Thailand, Laos, and Myanmar, every year from 2005 to 2022. Fires typically begin in northern Thailand and Myanmar in February, spread to northern Laos in March, decline by April and dissolve in May.

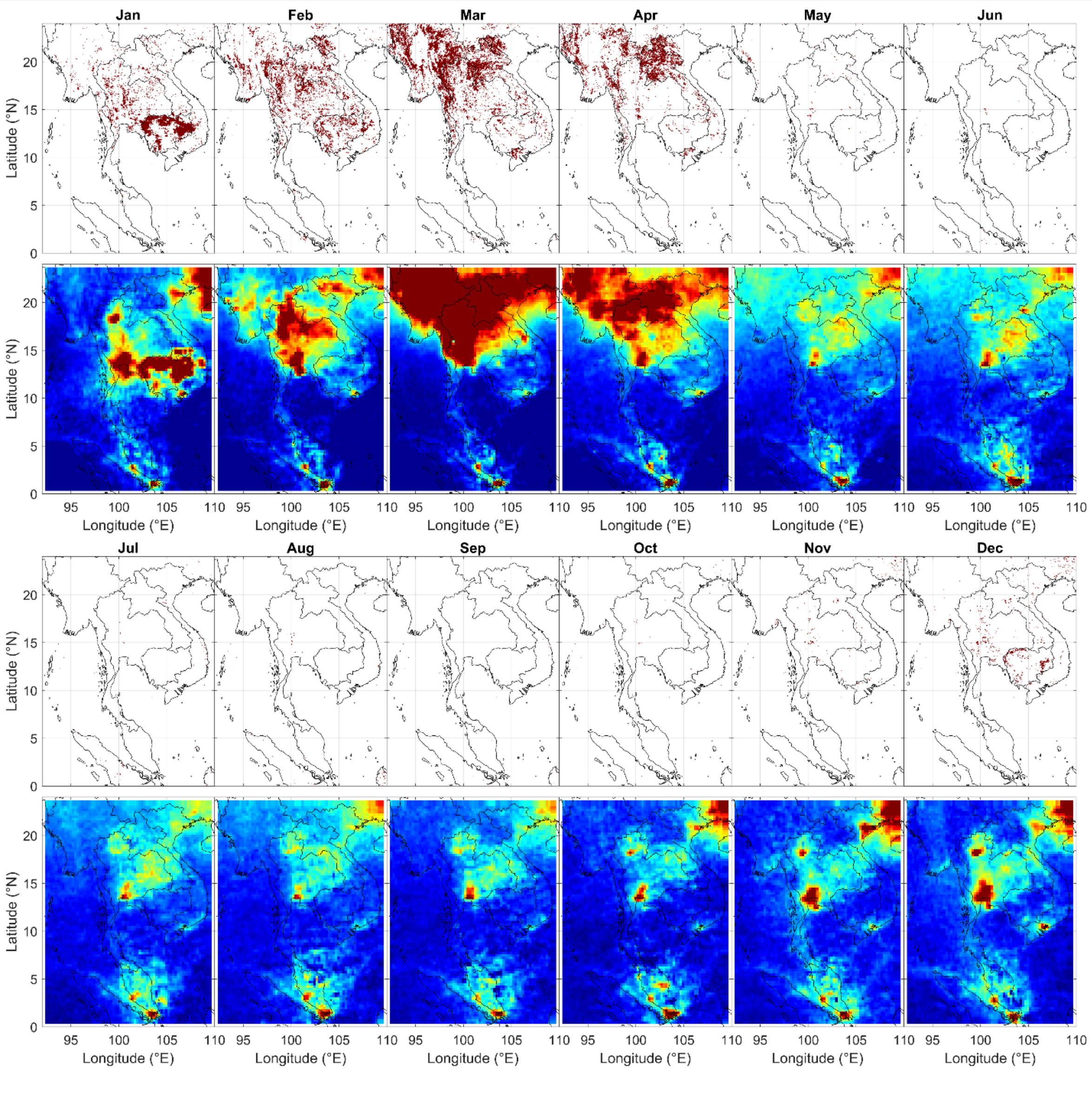

Figure 2: Monthly MODIS MCD64 burned area (1st and 3rd rows) and OMI tropospheric NO_2 column density (2nd and 4th rows, molecules cm^{-2}) over mainland Southeast Asia for the year 2007 (January to December, left to right and top to bottom)

Forest fires in Cambodia also continue to occur during this period but decrease in February and cease around March. As forest fires contribute to severe atmospheric pollution across 3-4 countries for 1-4 months each year over an 18-year period, they can be identified as one of the major contributors to NO_2 emissions in Southeast Asia. Additionally, to demonstrate the quantitative relationship between forest fires and atmospheric NO_2, we analyze two regions along the Thailand-Cambodia and Thailand-Myanmar borders (rectangles A and B in Figure 1(a)), as examples. Both regions are forested areas with no significant anthropogenic NO_2 emission sources. Thus, it can be inferred that forest fires are the predominant source of observed atmospheric NO_2 levels. Monthly data over 18 years show a significant correlation between burned area and NO_2 concentrations (Figure 3). Linear regression analysis indicates that each 500 × 500 m² burned pixel increases average NO_2 concentrations by approximately 4.0974 × 10^11 molecules/cm² in Cambodia and 3.4830 × 10^11 molecules/cm² in Myanmar. These differences may reflect variations in combustion conditions, biomass type, and moisture content.

ISSN: 1686-6576 (Printed) | ISSN 2673-0014 (Online) | © Geoinformatics International

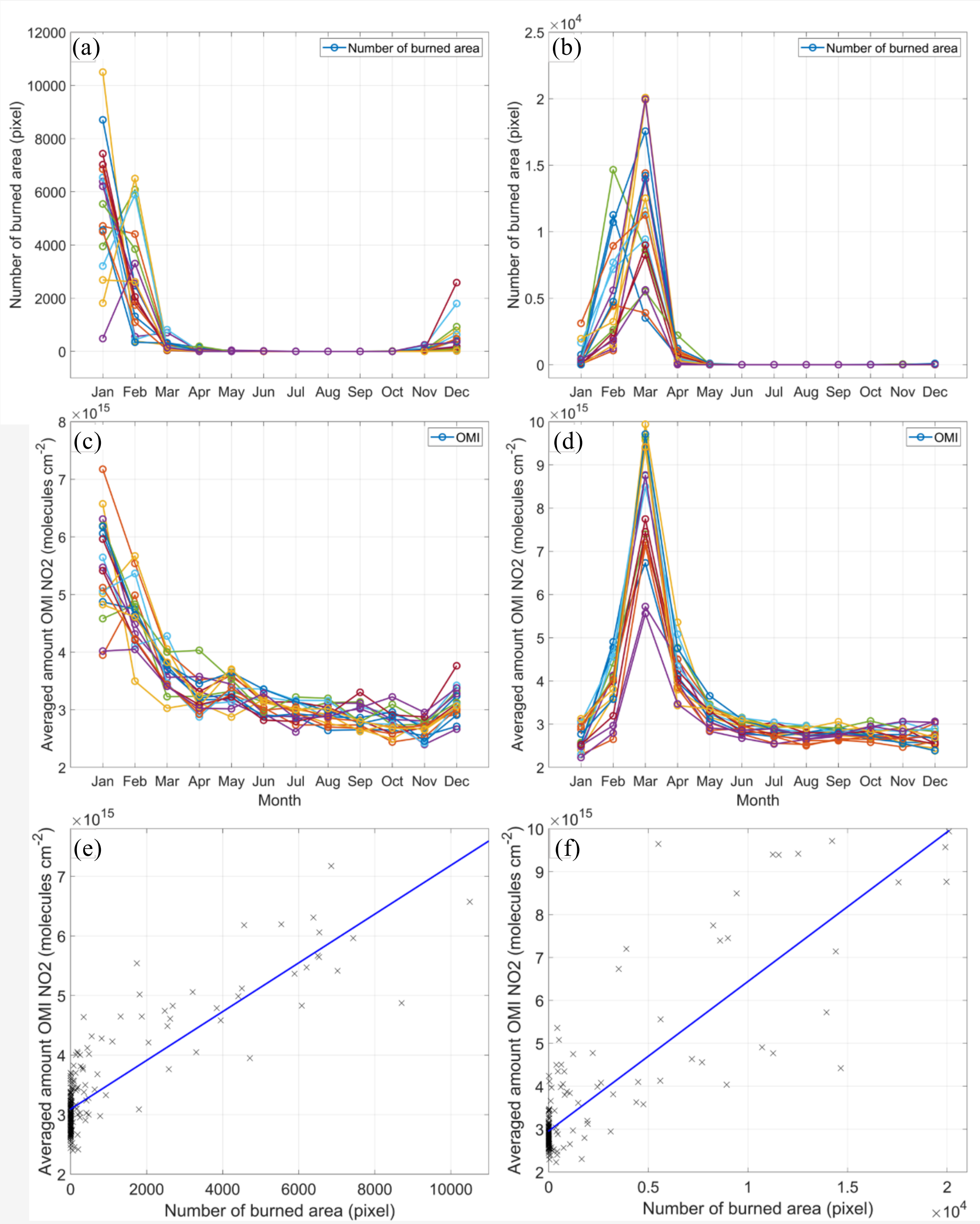

Figure 3: (a-b) Number of burned areas counts along the Thailand-Cambodia border (a) and Thailand-Myanmar border (b), corresponding to regions A and B in Figure 1(a). Each line represents a different year from the 18-year period (2005-2012). (c-d) Monthly variation in atmospheric NO_2 concentration over the same regions. (e-f) Scatterplots showing the relationship between the number of burned areas and the corresponding NO_2 concentrations including regression lines

During the May–July and August–October periods, NO_2 concentrations decline significantly, reaching their lowest levels in July and August (Figure 1(e)–(f)). This reduction is attributed to high precipitation and the absence of biomass burning. However, elevated NO_2 concentrations persist in urban areas, driven by continuous anthropogenic emissions. These seasonal maps clearly distinguish regions with year-round pollution from those affected primarily by seasonal biomass burning. In the following

ISSN: 1686-6576 (Printed) | ISSN 2673-0014 (Online) | © Geoinformatics International

sections, we conduct time-series analyses of NO_2 concentrations in the persistent hotspots across Southeast Asia to further investigate long-term trends and seasonal dynamics.

3.2.2 Time series decomposition

The boundaries of hotspot areas and key findings from the analysis are shown in Table 1. The median and mean NO_2 concentrations, derived from the trend component (T) which are unaffected by seasonal and random variability are calculated for each hotspot. The highest average NO_2 levels are observed over Singapore (6.68×10^{15} molecules/cm²), followed by Bangkok (6.21×10^{15}molecules/cm²), both of which are major urban centers characterized by dense traffic networks. The following areas are industrial zones such as the Mae Moh power plant in northern Thailand (5.39×10^{15}molecules/cm²) and Haiphong in Vietnam (5.30×10^{15}molecules/cm²), known for their extensive manufacturing activities, also exhibit elevated NO_2 concentrations. Urban areas including Hanoi (4.56×10^{15}molecules/cm²) and Kuala Lumpur (4.54×10^{15} molecules/cm²) show moderately high levels, though not as severe as the aforementioned locations. In contrast, Phnom Penh (2.91×10^{15}molecules/cm²), the capital of Cambodia, records the lowest NO_2 concentrations among the identified hotspots.

Seasonal analysis reveals that Bangkok and the Mae Moh power plant exhibit the most pronounced seasonal variation in Southeast Asia. Atmospheric NO_2 levels over Bangkok peak between November and January, a pattern attributed to the extended atmospheric lifetime of NO_2 during the cooler months. Similar seasonality is observed in Ho Chi Minh City. In contrast, coastal cities such as Singapore and Kuala Lumpur display minimal seasonal variation, with Singapore maintaining consistently high NO_2 levels throughout the year. Notably, although Bangkok has the second-highest average NO_2 levels, its strong seasonal fluctuations result in the highest concentrations in Southeast Asia during peak months (December–February).

A second group of hotspots is influenced by biomass burning, as discussed earlier. Forest fires in Cambodia, typically occurring in January, coincide with NO_2 peaks over Phnom Penh. Fires in northern Thailand, Laos, and Vietnam occur between February and April, aligning with the seasonal NO_2 maxima observed at the Mae Moh power plant (Thailand), Chiang Mai (Thailand), Hanoi (Vietnam), and Vientiane (Laos).

To access NO_2 concentration trend, we tabulate linear trend slopes before and after the COVID-19 pandemic to avoid the misinterpretation due to its disruption. In addition, we estimate NO_2 concentrations from the linear models for four key months: September 2005, December 2019, April 2020, and December 2022 to assess the impact of the COVID-19 pandemic on NO_2 emissions. These values help quantify the pandemic-induced decline and the extent of recovery.

Table 1: Time-series analysis of NO_2 concentrations over selected hotspots in Southeast Asia. Geographic boundaries are defined by the minimum and maximum latitude and longitude values for each location. Trend statistics such as means (Mean), medians (Med), and standard deviations (STD) are derived from the long-term trend component of the NO_2 time-series. Seasonal amplitude (Amp), which are the differences between the maximum and minimum values, represents the average annual variation in NO_2 levels. Linear regression slopes are calculated separately for the pre-COVID (September 2005-December 2019) and post-COVID (April 2020-December 2022) periods. Estimated NO_2 concentrations at the start and end of each period are derived from the fitted linear models and presented in the NO_2 concentrations columns

No.	City	Longitude		Latitude		Trend			S	Linear Models					
										Slope		NO_2 concentrations			
		Min	Max	Min	Max	Med	Mean	STD	Amp	2005-2019	2020-2022	2005	2019	2020	2022
		Degrees				10^{15} molecules/cm^2				10^{15} molecules/cm^2/yr		10^{15} molecules/cm^2			
1	Bangkok	100.27	100.90	13.60	13.90	6.21	6.26	0.31	5.21	-0.0294	0.0225	6.56	6.14	5.77	5.82
2	ChiangMai	98.73	99.23	18.54	19.04	3.94	3.89	0.21	3.96	0.0290	-0.2432	3.70	4.12	4.03	3.52
3	MaeMoh	99.80	99.90	18.30	18.70	5.39	5.33	0.30	5.75	0.0039	-0.2526	5.37	5.43	5.22	4.69
4	Kuala Lumpur	101.44	101.94	2.80	3.20	4.54	4.55	0.33	0.64	-0.0213	0.4205	4.76	4.46	3.84	4.72
5	Singapore	103.60	103.90	1.30	1.60	6.68	6.58	0.67	1.91	-0.0285	0.5900	7.02	6.61	4.72	5.95
6	Ho Chi Minh	106.62	106.90	10.60	10.90	3.70	3.71	0.15	1.58	0.0307	-0.0361	3.48	3.92	3.77	3.70
7	Hanoi	105.87	105.88	20.87	21.20	4.56	4.53	0.41	2.77	0.0896	-0.0822	3.83	5.11	4.97	4.80
8	Haiphong	106.60	106.90	20.87	21.20	5.30	5.10	0.64	2.80	0.1373	0.1242	4.01	5.97	5.56	5.82
9	Phnom Penh	104.67	105.17	11.32	11.82	2.91	2.96	0.15	1.34	0.0184	0.1062	2.80	3.06	3.06	3.28
10	Vientiane	102.35	102.85	17.72	18.22	3.80	3.78	0.21	2.90	0.0304	-0.1009	3.55	3.99	3.92	3.71
11	Mandalay	95.83	96.33	21.73	22.23	3.46	3.42	0.18	3.50	0.0338	-0.0894	3.16	3.65	3.61	3.42
12	Naypyitaw	95.87	96.37	19.50	20.00	3.44	3.41	0.21	4.20	0.0352	-0.1507	3.15	3.66	3.61	3.30

ISSN: 1686-6576 (Printed) | ISSN 2673-0014 (Online) | © Geoinformatics International

To make a more in-depth analysis of the hotspots, the results from the time-series decomposition will be used to make diagrams. For each of the hotspots, four diagrams are constructed. The first diagram shows monthly mean NO_2 concentrations from 2005-2022. The second diagram presents monthly trend components (T) with fitted linear, quadratic, and cubic regression models for the same period. The third diagram plots the residuals (r) between the observed data and the sum of the trend and seasonal components for the same period. The fourth diagram shows the monthly seasonal components (S) with error bars indicating ±1 standard deviation for all twelfth months across years.

In our research, the diagrams have been made for all the hotspots. However, for the sake of conciseness, some of the diagrams are not shown here. The long-term linear trend indicates a decline in atmospheric NO_2 concentrations over Bangkok (Figure 4(b)). The trend can be divided into two distinct periods. A pre-pandemic period from 2005 to 2020 indicates a decreasing trend. A post-pandemic period from 2020 to 2022 shows a slight increase, but levels had not returned to pre-pandemic values by the end of 2022. Chiang Mai (Figure 5(b)) and the Mae Moh power plant (Figure 6(b)) in northern Thailand exhibit a similar long-term trend.

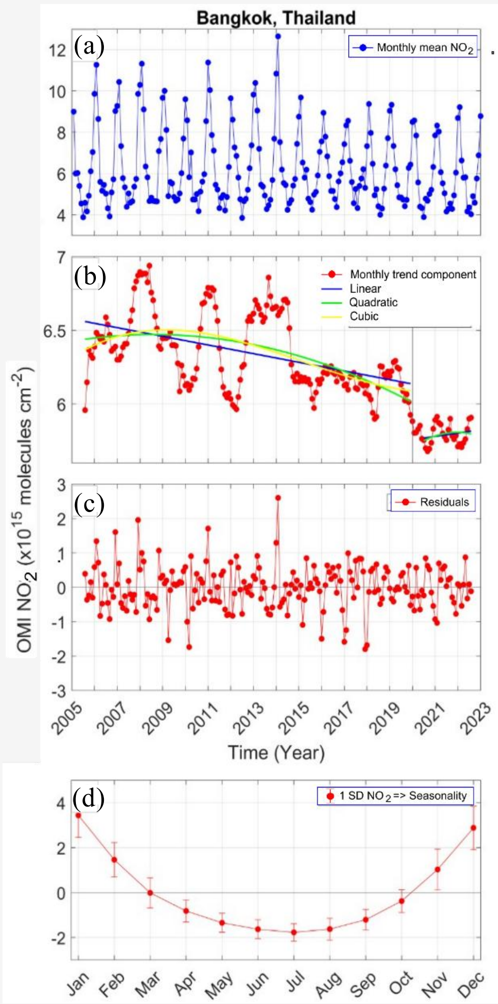

Figure 4: Time-series decomposition of atmospheric NO_2 concentration over Bangkok, Thailand: (a) Monthly mean NO_2 concentrations from 2005-2022. (b) Monthly trend component (T) with fitted linear, quadratic, and cubic regression models. (c) Residuals (r) between the observed data and the sum of the trend and seasonal components. (d) Monthly seasonal components (S) with error bars indicating ±1 standard deviation across years

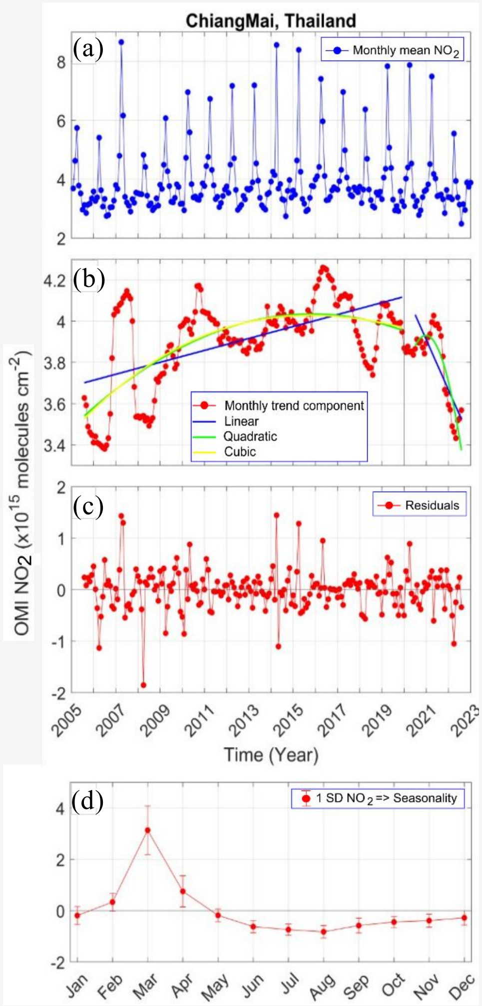

Figure 5: Time-series decomposition of atmospheric NO_2 concentration over Chiang Mai, Thailand: (a) Monthly mean NO_2 concentrations from 2005-2022. (b) Monthly trend component (T) with fitted linear, quadratic, and cubic regression models. (c) Residuals (r) between the observed data and the sum of the trend and seasonal components. (d) Monthly seasonal components (S) with error bars indicating ±1 standard deviation across years

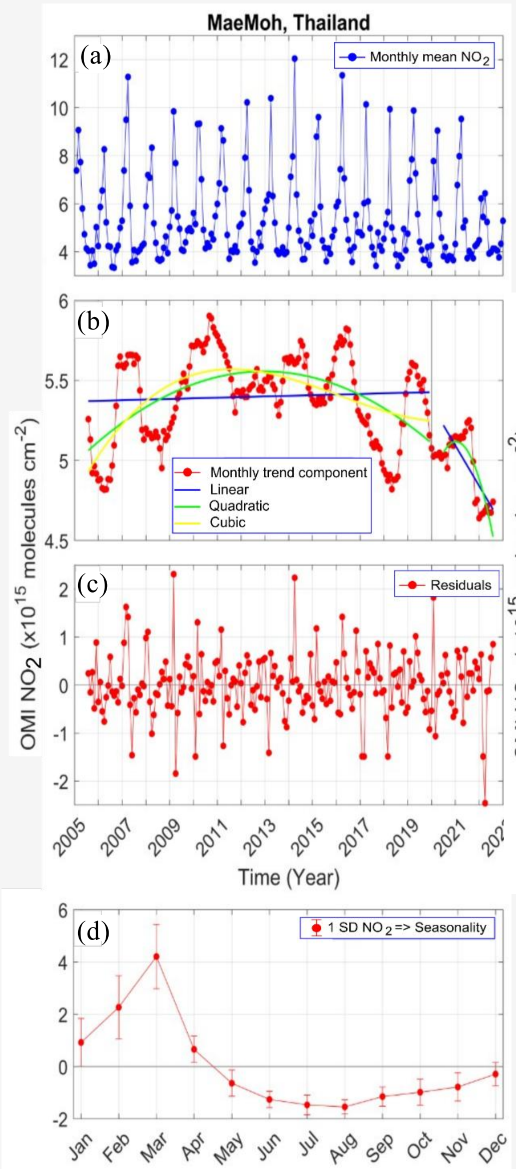

Figure 6: Time-series decomposition of atmospheric NO_2 concentration over Mae Moh, Thailand: (a) Monthly mean NO_2 concentrations from 2005-2022. (b) Monthly trend component (T) with fitted linear, quadratic, and cubic regression models. (c) Residuals (r) between the observed data and the sum of the trend and seasonal components. (d) Monthly seasonal components (S) with error bars indicating ±1 standard deviation across years

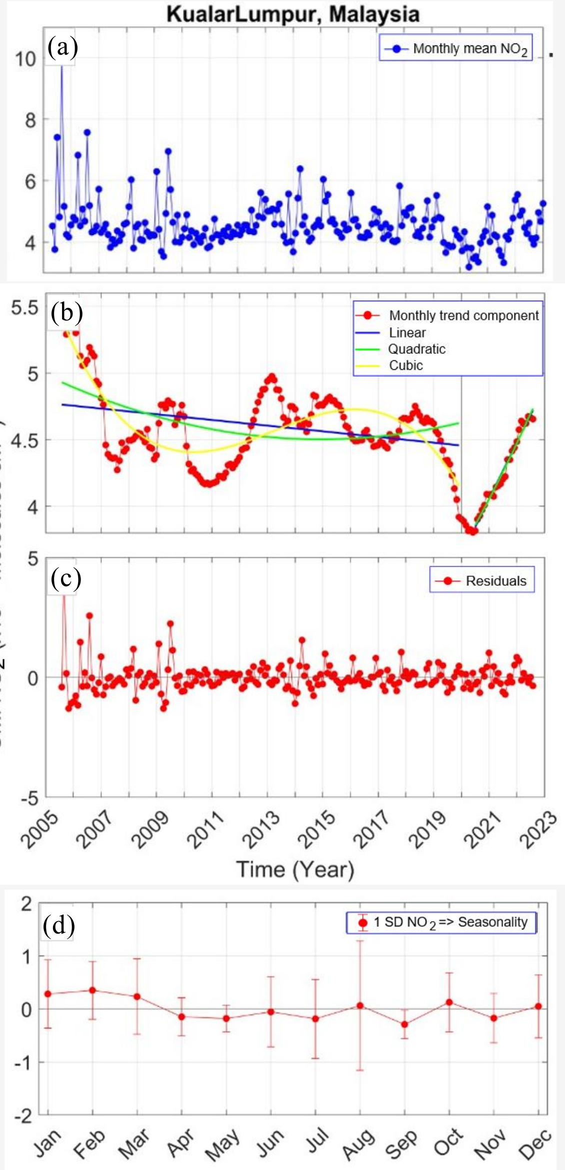

Figure 7: Time-series decomposition of atmospheric NO_2 concentration over Kuala Lumpur, Malaysia: (a) Monthly mean NO_2 concentrations from 2005-2022. (b) Monthly trend component (T) with fitted linear, quadratic, and cubic regression models. (c) Residuals (r) between the observed data and the sum of the trend and seasonal components. (d) Monthly seasonal components (S) with error bars indicating ±1 standard deviation across years

However, NO_2 concentrations drop during the pandemic and continue to decline significantly afterward. Non-linear trends appear to illustrate the time-series data more precisely compared to linear regression. In Kuala Lumpur and Singapore (Figure 7 and Figure 8), NO_2 levels declined slightly before the pandemic and dropped significantly during it by 0.62×10^{15} and 1.89×10^{15} molecules/cm², respectively. This suggests that the shutdown of human activities had a substantial impact on Singapore, as the decline was the highest in Southeast Asia. Following the pandemic, atmospheric NO_2 levels increased significantly in both areas, forming a V-shaped pattern with a bottom around mid-2020. Due to a smaller decrease over Kuala Lumpur, NO_2 levels rebounded to slightly higher levels than pre-pandemic by the end of 2022. However, NO_2 concentrations over Singapore remain lower than their pre-pandemic levels. Noteworthy increases in NO_2 concentrations were observed over major cities in Vietnam from 2005 to 2020, including Ho Chi Minh City, Hanoi (Figure 9), and especially Haiphong (Figure 10), which are industrial areas.

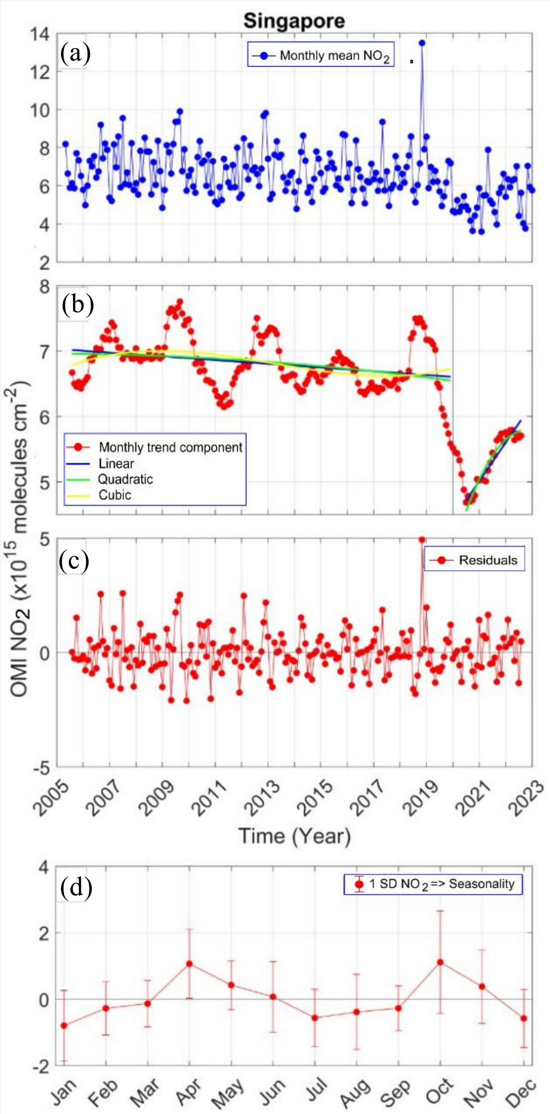

Figure 8: Time-series decomposition of atmospheric NO_2 concentration over Singapore: (a) Monthly mean NO_2 concentrations from 2005-2022. (b) Monthly trend component (T) with fitted linear, quadratic, and cubic regression models. (c) Residuals (r) between the observed data and the sum of the trend and seasonal components. (d) Monthly seasonal components (S) with error bars indicating ±1 standard deviation across years

.

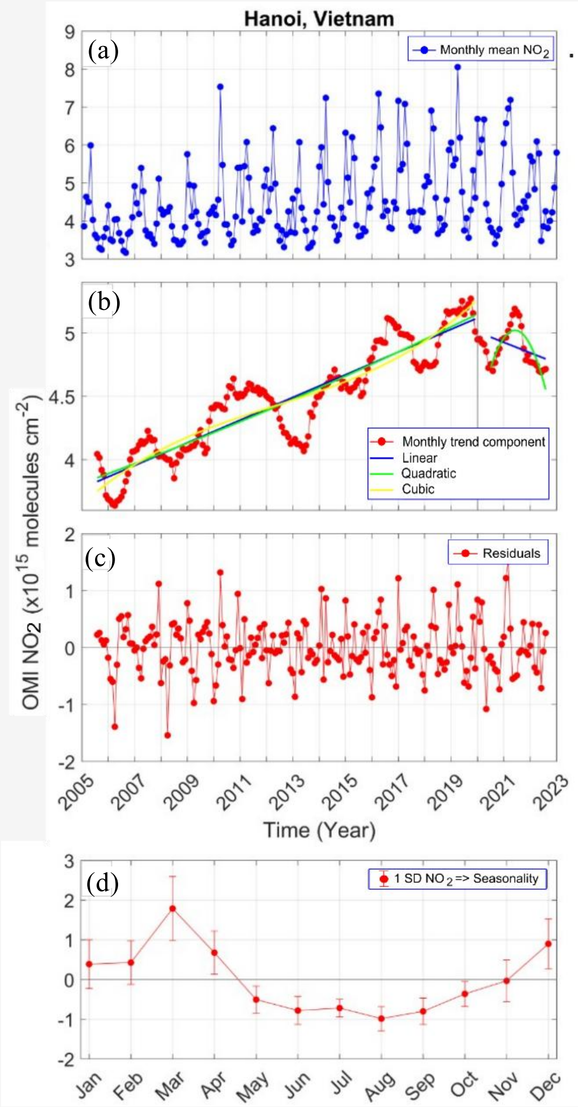

Figure 9: Time-series decomposition of atmospheric NO_2 concentration over Hanoi, Vietnam: (a) Monthly mean NO_2 concentrations from 2005-2022. (b) Monthly trend component (T) with fitted linear, quadratic, and cubic regression models. (c) Residuals (r) between the observed data and the sum of the trend and seasonal components. (d) Monthly seasonal components (S) with error bars indicating ±1 standard deviation across years

These cities experienced the most rapid growth in Southeast Asia, consistent with the country's industrial expansion. While Ho Chi Minh City and Hanoi saw declines post-pandemic, Haiphong's NO_2 levels only slightly dropped during the pandemic before resuming a similar growth rate as before. NO_2 concentrations over Nay Pyi Taw and Mandalay in Myanmar (Figure 11), Phnom Penh in Cambodia, and Vientiane in Laos show trends best captured by non-linear models. These cities experienced early increases in NO_2 during the pre-pandemic period. The pandemic did not cause a significant drop in NO_2 levels in these locations. While the NO_2 concentration in Phnom Penh increased with a steeper slope than before the pandemic, the other three cities experienced declining trends.

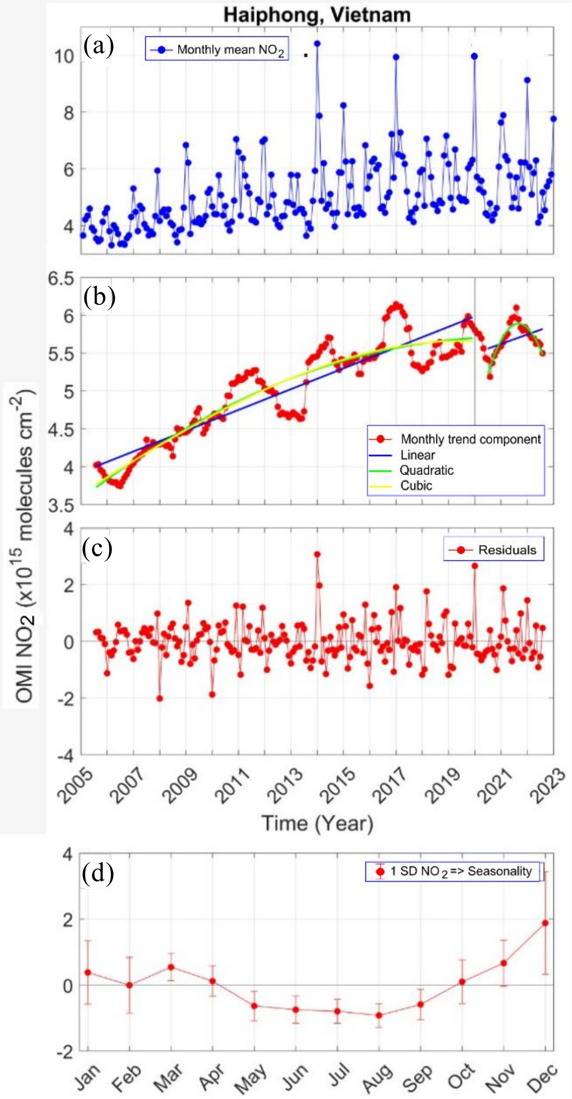

Figure 10: Time-series decomposition of atmospheric NO_2 concentration over Haiphong, Vietnam. (a) Monthly mean NO_2 concentrations from 2005-2022. (b) Monthly trend component (T) with fitted linear, quadratic, and cubic regression models. (c) Residuals (r) between the observed data and the sum of the trend and seasonal components. (d) Monthly seasonal components (S) with error bars indicating ±1 standard deviation across years

.

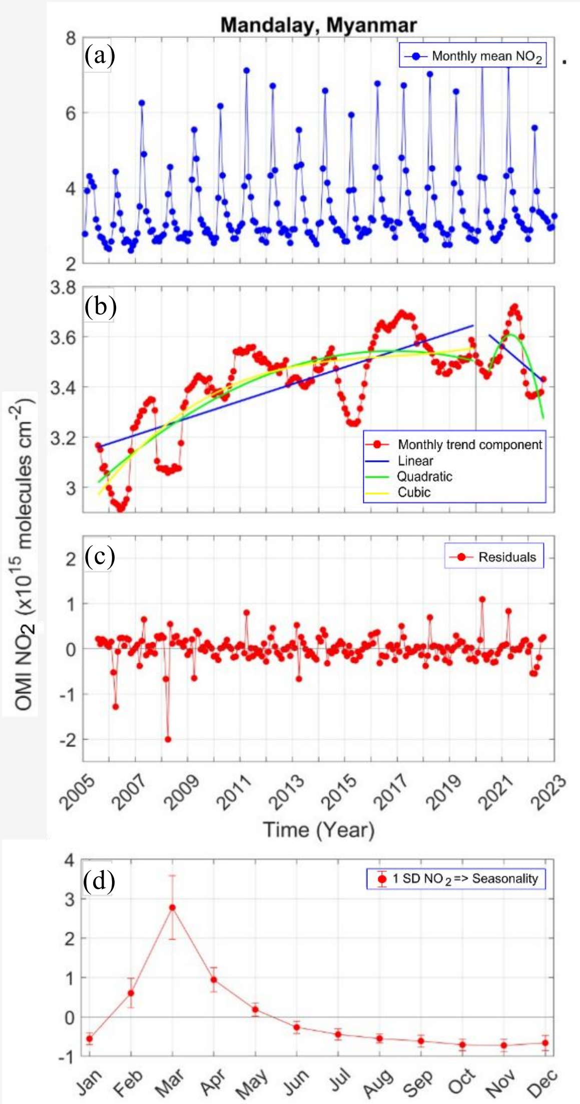

Figure 11: Time-series decomposition of atmospheric NO_2 concentration over Mandalay, Myanmar. (a) Monthly mean NO_2 concentrations from 2005-2022. (b) Monthly trend component (T) with fitted linear, quadratic, and cubic regression models. (c) Residuals (r) between the observed data and the sum of the trend and seasonal components. (d) Monthly seasonal components (S) with error bars indicating ±1 standard deviation across years

.

ISSN: 1686-6576 (Printed) | ISSN 2673-0014 (Online) | © Geoinformatics International

4. Maps of NO_2 Emissions in Southeast Asia

In the previous section, we analyze long-term NO_2 levels to evaluate and describe the NO_2 variations across Southeast Asia using NO_2 concentration maps. However, since NO_2 remains in the atmosphere for a period of time after emission, typically less than 24 hours [4][37] and [52] it is transported by wind currents during its existence. As a result, NO_2 concentration maps often reflect the distribution of transported NO_2 plumes rather than the precise locations of emission sources. Moreover, the temporal averaging used to generate monthly mean concentrations introduces additional spatial dispersion or blurring due to variability in wind speed and direction. For regulatory and mitigation purposes, emission maps are more informative than concentration maps, as they more accurately identify the locations of emission sources.

To address this, we apply the flux divergence method, which combines satellite-derived NO_2 vertical column density (VCD) data with wind field information to estimate the spatial distribution of NO_2 emissions across Southeast Asia. This method has proven effective in identifying emission sources in various regional and global studies [32][37][50][51] and [53].

4.1 Methodology

The TROPOMI L2 products are used to compute NO_2 flux divergence. The analysis focuses on the October–January period from 2018 to 2022, selected for its high NO_2 concentrations and strong correlation with ground-based observations. Due to the typically high noise in flux divergence calculations, temporal averaging is essential. To maximize the signal-to-noise ratio, we calculate the mean flux divergence by averaging the entire dataset (October-January 2018-2022). We first resample the swath based TROPOMI L2 products onto a 2-kilometer geographic grid to facilitate temporal averaging. Notably, the spatial resolution of TROPOMI improved from 7×3.5 km² to 5.5×3.5 km² after August 2019. This inhomogeneity is mitigated through the resampling process, which maps all observations onto a common regular grid. Differences in native pixel sizes, together with the irregular spatial overlap of satellite swaths, are naturally smoothed during the resampling procedure. In addition, the larger number of observations acquired after the resolution improvement increases the sampling density, thereby enhancing the representation of finer spatial structures. Consequently, the impact of the resolution change on the derived flux divergence fields is expected to be minor and does not require additional correction.

For each daily scene, only pixels with a quality assurance (QA) value greater than 0.5 are retained, following the recommendation of [54]. This threshold is more relaxed than the commonly used value of 0.75 for strictly cloud-free conditions, allowing for greater data retention in regions with frequent cloud contamination such as Southeast Asia. Given the tropical climate of the region, where persistent cloud cover can significantly limit data availability, the analysis is restricted to the October–January period, when cloud occurrence is relatively lower. In this study, approximately half of the observations are retained after QA filtering. Water areas are excluded using surface classification parameters provided in the TROPOMI L2 products. We then apply oversampling using a 2-kilometer grid, which is finer than the original TROPOMI L2 product resolution. Previous studies have demonstrated that this finer resolution enhances the characterization of emission sources. To address missing data, we apply a 3×3 pixel moving average filter to interpolate missing grid cells. This localized interpolation method avoids extrapolation errors caused by persistent cloud cover in the region. Since daily data often contains unreliable pixels due to widespread cloudiness, we exclude these cloudy grid cells when computing the average to prevent bias from low observation counts. The resulting daily dataset will be combined with wind data to compute daily NO_2 flux divergence.

NO_2 fluxes (f) are computed by multiplying NO_2 VCDs (d) with horizontal wind vectors (w), following the approach of [50] using Equation 2:

$$f = dw$$

Equation 2

This calculation defines NO_2 transport, representing the horizontal flow rate of NO_2 at specific pixels. According to [50], the spatial derivative of the NO_2 flux, known as flux divergence, quantifies the net emission or removal of NO_2 within a grid cell. The flux divergence is defined in Equation 3:

$$\nabla f = \frac{\partial f^E}{\partial E} + \frac{\partial f^N}{\partial N} = Emission\ -\ Sinking$$

Equation 3

Where:

∇f = flux divergence

f^E = the flux in east-west direction

f^N = the flux in north-south direction

In an area with constant wind speed and direction, if there is no emission or sinking, the NO_2 flux should flow into and out of the pixel equally. Therefore, any divergence indicates a change in NO_2 levels within that specific area. A positive divergence indicates that emissions exceed sinking in the area, while a negative divergence indicates the opposite. Since the satellite-derived NO_2 flux field is defined on a discrete grid, flux divergence is estimated numerically using a finite-difference approach. A fourth-order central difference scheme is employed to improve numerical accuracy [50]. This calculation is performed as a sum of the divergence in both east and north directions as shown in Equation 4:

$$\nabla_{4,n} \cdot f^{n}_{(e,n)} = \frac{f^{E}_{(e-2,n)} - 8 f^{E}_{(e-1,n)} + 8 f^{E}_{(e+1,n)} + f^{E}_{(e+2,n)}}{12\Delta x} + \frac{f^{N}_{(e,n-2)} - 8 f^{N}_{(e,n-1)} + 8 f^{N}_{(e,n+1)} + f^{N}_{(e,n+2)}}{12\Delta y}$$

Equation 4

Where:

$\nabla_{4,n} \cdot f^{n}_{(e,n)}$ = Flux divergence computed using a fourth-order central difference scheme at grid cell (i, j)

$f^{E}_{(a,b)}$ = Eastward NO_2 flux at grid cell (i, j)

$f^{N}_{(a,b)}$ = Northward NO_2 flux at grid cell (i, j)

Δx = Length of a grid cell in the east-west direction

Δy = Length of a grid cell in the north-south direction

The letters e and n denote the pixel index in east-west and north-south directions, respectively. As illustrated by the above equation, the flux divergence method can be used to investigate emission rates if the *Singking* term (in Equation 3), representing chemical loss and deposition, is known beforehand. However, the *Singking* term is not considered in our calculations. This omission can help better localize emission sources, as demonstrated by [43], which can identify emission sources with clear boundaries as the *Singking* term can cause smearing and reduce spatial detail of emission sources. However, excluding this term leads to an underestimation of emission rates. Previous studies suggest that typical NO_2 lifetimes range from approximately 4 to 9 hours [37][55] and [56], and sensitivity analyses indicate that neglecting the *Sinking* term can lead to differences in emission estimates of about 25% [32]. Incorporating the *Sinking* term would require reliable estimates of NO_2 lifetime, which vary significantly depending on local meteorological and chemical conditions and remain insufficiently constrained across Southeast Asia. Given that the primary objective of this study is to map spatial emission patterns rather than to derive highly accurate quantitative emission estimates, the omission of the *Sinking* term is considered acceptable. In this context, flux divergence plays a more important role in identifying emission hotspots, while inclusion of the *Sinking* term may obscure smaller sources.

The final emission maps are generated by averaging the flux divergence values across all valid observations during the study period. Note that the flux of NO_2 is not converted to the flux of NO_x, as our objective is to identify NO_2 emission sources rather than to quantify total emissions. The absence of upscaling does not impact the identification of emission hotspots. Moreover, the NO_x-to-NO_2 conversion factor in Southeast Asia remains uncertain and may differ from values reported in previous studies [37] and [50]. As such, this factor is not addressed in the present analysis.

4.2 Results and Discussion

This subsection presents detailed results and discussion, organized into four parts. The first part provides an overview of the findings over Southeast Asia, followed by an in-depth analysis of three specific areas: Bangkok Metropolitan Region, Northern Vietnam Industrial Corridor, and Singapore and Kuala Lumpur. To support the identification of emission source locations of these three areas, two established emission inventories are used as references. The first is the Global Power Plant Database (v1.3.0) [57], an open- access database from the World Resources Institute. This database details power plants worldwide, including their locations, capacities, and primary fuel types. For this study, plants with capacities exceeding 0.5 GW and primary fuels relevant to NO_2 emissions, such as coal, gas, and oil are in our focus. The second inventory is the EDGAR version 5.0 Global Air Pollutants emission inventory [58]. This dataset provides global NO_2 emissions in 0.1˚x0.1˚ grid cells and is divided into multiple layers corresponding to different types of emission sources. According to the dataset, Public Power, Industry, and Transport are the primary sources of NO_2 emissions in Southeast Asia. In this discussion, we include grid cells with total NO_2 emissions exceeding 1 kiloton/year and present them with different symbols to represent stationary (Public Power and Industry) and non-stationary (Transport) sources. Symbols are categorized into three shapes based on the dominant emission source in each grid cell: stationary sources (Public Power and Industry), non-stationary sources (Transport), and combined sources (Public Power and/or Industry and Transport). Note that emissions from biomass burning are not included in these inventories and are therefore not assessed here.

4.2.1 Overall Southeast Asia

Figure 12(a) is a plot of the averaged atmospheric NO_2 concentrations covering mainland Southeast Asia. Alongside, Figure 12(b), is the plot of the computed NO_2 flux divergences derived from the same TROPOMI dataset. The figures indicate that many coastal cities in Southeast Asia experience high NO_2 concentrations, as identified as hotspots in the previous section, significantly influenced by wind transport, resulting in spatial smearing that obscures the precise locations of emission sources. However, the flux divergence maps reveal more localized and distinct emission patterns. This is particularly noteworthy given that the flux divergence technique has not been widely applied to coastal regions, where meteorological conditions probably differ from those in previously studied inland areas.

4.2.2 Bangkok Metropolitan region

Figure 13 presents the analysis for the Bangkok Metropolitan Region, home to over 17.4 million people. The information from the Global Power Plants Database and EDGAR inventory are mapped as squares and other symbols, respectively, in Figure 13(b).

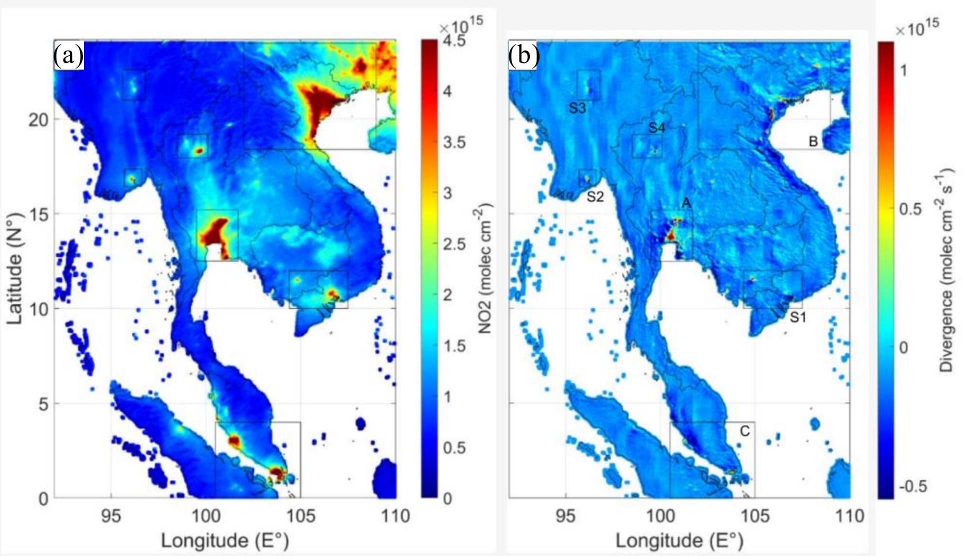

Figure 12: (a) Average atmospheric NO_2 concentrations map derived from TROPOMI dataset (October–January 2018–2022**)**. (b) Mean NO_2 flux divergence map. Rectangles A, B, and C correspond to the detailed case studies shown in Figures 13, 14, and 15, respectively

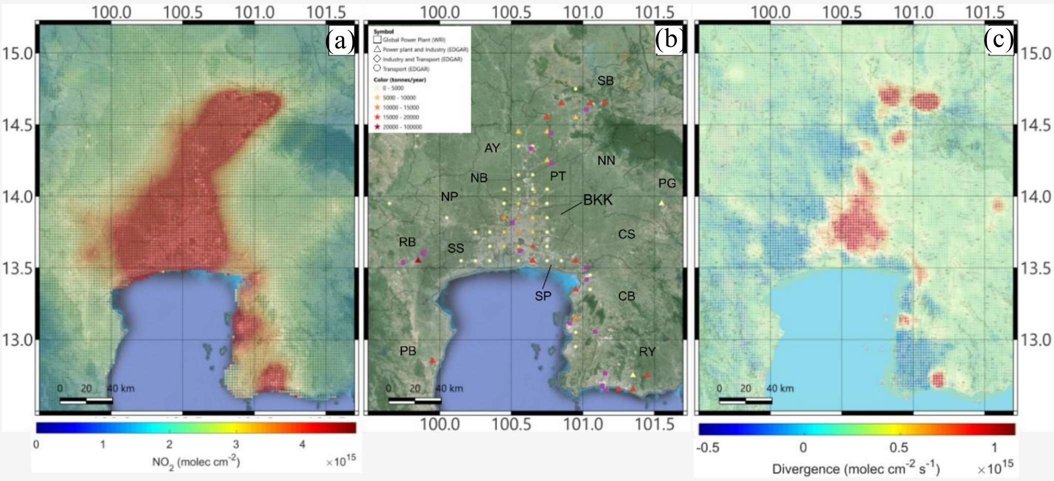

Figure 13: (a) NO_2 concentrations derived from TROPOMI dataset (October–January 2018–2022**)** over central Thailand. (b) Emission source locations from the Global Power Plant Database (squares) and EDGAR (other symbols). Symbol colors indicate the amount of gas emissions. (c) NO_2 flux divergence map. A positive divergence (red) indicates a high-emission region, whereas a negative divergence (blue) indicates a region with more NO_2 entering than exiting

ISSN: 1686-6576 (Printed) | ISSN 2673-0014 (Online) |

Symbol colors indicate the amount of gas emissions. The thin black lines represent provincial boundaries: AY: Ayutthaya; BKK: Bangkok; CB: Chonburi; CS: Chachoengsao; NB: Nonthaburi; NN: Nakhon Nayok; NP: Nakhon Pathom; PB: Phetchaburi; PG: Prachin Buri; PT: Pathum Thani; RB: Ratchaburi; RY: Rayong; SB: Saraburi; SP: Samut Prakan; SS: Samut Sakhon. This map indicates that Bangkok is highly congested, particularly in its city center, and exhibits elevated NO_2 emissions exceeding 1 kiloton per year. The EDGAR inventory identifies high NO_2 emissions (>1 kt/year) concentrated in the city center, mostly from transportation. The spatial extent of these emissions appears to align with urban expansion patterns. The inventories also identify several significant industrial estates located outside of Bangkok. The average NO_2 concentrations observed by TROPOMI (Figure 13(a)) are elevated across the region; however, pinpointing specific emission sources is challenging due to the effect of wind-driven smearing. This phenomenon causes NO_2 plumes to disperse and overlap, blending emissions from two distinct clusters: one originating from traffic and manufacturing activities in central Bangkok, and the other from industrial facilities and power plants located to the north of the city. This results in a single, diffuse concentration patch that obscures the spatial distinction between individual emission sources. Figure 13(c) represents NO_2 flux divergence map. A positive divergence (red) indicates a high-emission region, where more NO_2 is exiting than entering, whereas a negative divergence (blue) indicates a region with more NO_2 entering than exiting. Maps were generated using QGIS Desktop 3.22.2 and Google Satellite Basemap. Contrary to the concentration map, the flux divergence map mitigates most of the wind-driven smearing effects and reveals distinct emission zones. The spatial extent of concentrated divergences closely matches the urban footprint and aligns well with EDGAR transport and industrial emission zones. This result demonstrates that the flux divergence technique effectively captures NO_2 emission sources, not only from point sources but also from complex spatial patterns such as Bangkok's urban expansion. Moreover, it successfully identifies emissions from power plants and industrial areas located north of Bangkok sources that are obscured in the NO_2 concentration map.

4.2.3 Northern Vietnam Industrial Corridor

Figure 14: (a) NO_2 concentrations derived from TROPOMI dataset (October–January 2018–2022) over northern Vietnam focuses on the northern economic zone of Vietnam, encompassing Hanoi and the surrounding provinces of Bac Ninh, Hai Duong, Hung Yen, Hai Phong, and Thai Binh. This region is one of Vietnam's largest industrial clusters. Figure 14(a) displays NO_2 concentrations over northern Vietnam, including Hanoi and surrounding provinces. Figure 14(b) shows the terrain by plotting topographic elevations from the SRTM DEM dataset. The information from the Global Power Plants Database and EDGAR inventory are mapped as squares and other symbols, respectively, in Figure 14(c). Symbol colors display amount of gas emissions. Blue lines represent main rivers [59]. The NO_2 flux divergence map is shown in Figure 14(d). Positive values (red) indicate net emission zones, while negative values (blue) indicate net inflow regions. Figure 14(e)–(g) presents transect profiles of NO_2 concentrations from south to north (locations shown in Figure 14(a)). Figure 14(h)–(j) renders the three corresponding topographic profiles. Vertical black lines mark elevation peaks surrounding the center of the profiles. The profiles are centered around the NO_2 peak. Maps were generated using QGIS Desktop 3.22.2 and Google Satellite Basemap.

Similar to the Bangkok area, wind significantly impacts the identification of emission sources. TROPOMI NO_2 concentration maps show widespread elevated levels across the region. This makes it challenging to distinguish between different emission sources. The flux divergence map (Figure 14(d)), however, reveals that the most significant emissions originate from sources near the shoreline. This indicates that atmospheric NO_2 emissions are not distributed across the area, as depicted by the NO_2 concentration map, but are instead concentrated in coastal industrial zones, with wind dispersing the pollutants inland across the region. Although some significant emission sources are found inland, away from the coastlines, their significance is not comparable to those near the shoreline. Furthermore, despite the observations representing NO_2 levels in the atmosphere accumulated from satellite to ground (~700 km), we find that the spatial extent of high NO_2 concentrations relates to topography. To further investigate the influence of topography on NO_2 dispersion, we use elevation data from the Shuttle Radar Topography Mission (SRTM), down sampled from its original 30-meter resolution to a 2-kilometer grid size to align with our NO_2 analysis (Figure 14(b)). According to the topography, the spatial extent of high NO_2 concentrations aligns with low-lying terrain. Specifically, the spatial extent of the blown NO_2 concentration appears bounded by the elevated landforms surrounding the plateau. These high NO_2 concentrations seem to flow in a single line to the north, tracing the path of the Red River, which flows through a mountainous gorge.

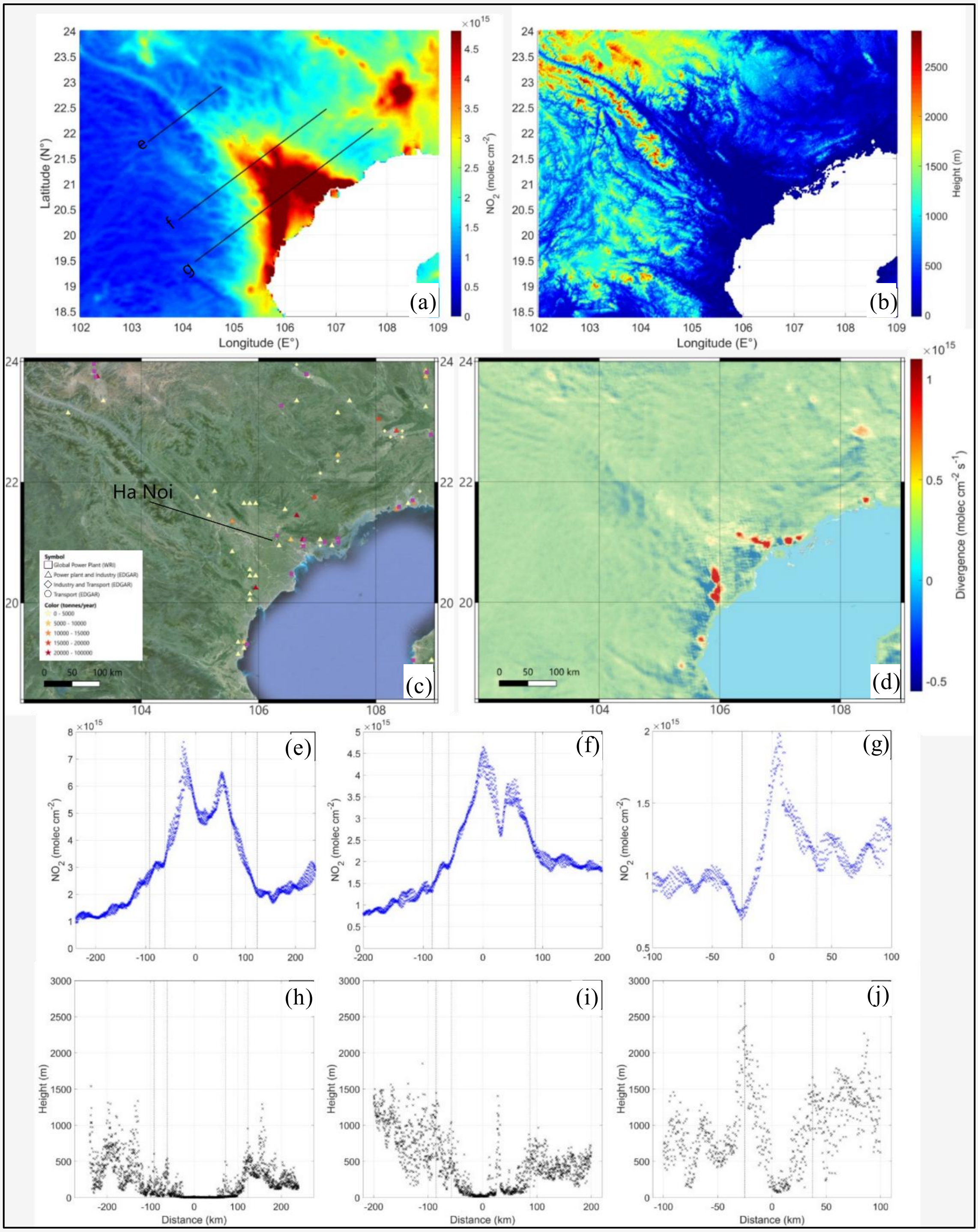

Figure 14: (a) NO_2 concentrations derived from TROPOMI dataset (October–January 2018–2022**)** over northern Vietnam. (b) Topographic elevation from the SRTM DEM dataset. (c) Emission source locations from the Global Power Plant Database (squares) and EDGAR (other symbols). Symbol colors indicate the amount of gas emissions (e) to (g) transect profiles of NO_2 concentrations from south to north, (h) to (j) corresponding topographic profiles

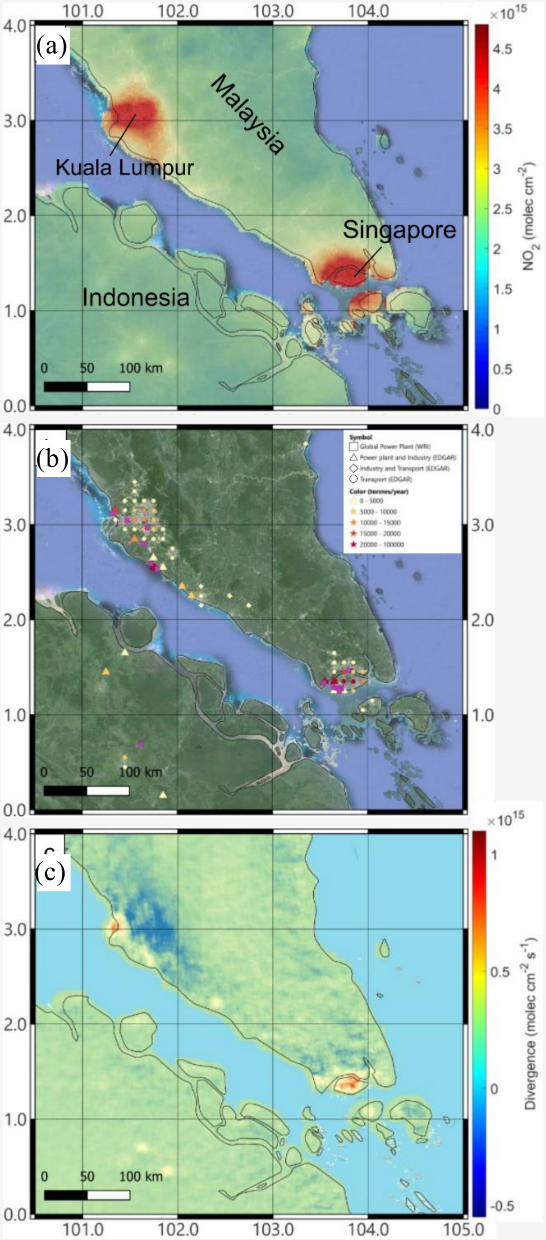

Figure 15: (a) NO_2 concentrations derived from TROPOMI dataset (October–January 2018–2022**)** over Malaysia and Singapore. (b) Emission source locations from the Global Power Plant Database (squares) and EDGAR (other symbols). Symbol colors indicate the amount of gas emissions. (c) NO_2 flux divergence map. A positive divergence (red) indicates a high-emission region, whereas a negative divergence (blue) indicates a region with more NO_2 entering than exiting

This could be attributed to the topography of the gorge acting as a natural barrier for containing atmospheric NO_2. Alternatively, it could be due to the presence of a road along the river. This ambiguity, however, requires further investigation. To further investigate the role of topography in shaping NO_2 dispersion patterns, we present three transect profiles of NO_2 concentrations and elevation, with locations indicated in Figure 14(a). Each profile is centered on areas of high NO_2 concentration, aligned with the origin ($x = 0$) of the horizontal axis. Vertical black lines mark the positions of elevation peaks along each transect.

The profiles reveal that the highest NO_2 concentrations are generally confined within the first or second topographic peaks to the east and west of the central region. This pattern suggests that elevated terrain acts as a natural barrier, containing NO_2 within plateau regions. In the southernmost profile, NO_2 concentrations are bounded by peaks approximately 500 meters in height. The second profile from the south shows a similar pattern, with surrounding peaks ranging from 700 to 1000 meters. Additionally, a localized drop in NO_2 concentration is observed in the central region, coinciding with significant topography (~1100 meters) in the central region. In the northernmost profile, located near the entrance to a gorge, NO_2 concentrations are similarly confined by the first topographic peaks on either side. These findings reveal data that can provide information on the height of the top layers of NO_2 concentration in the atmosphere and potentially vertical distribution of NO_2. However, this investigation is beyond the scope of this study and the results demonstrate the potential for future research.

4.2.4 Singapore and Kuala Lumpur

Figure 15 focuses on coastal cities of Singapore and Kuala Lumpur. NO_2 concentration map is shown in Figure 15(a). The information from the Global Power Plants Database and EDGAR inventory are mapped as squares and other symbols, respectively, in Figure 15(b). Symbol colors indicate the amount of gas emissions. Figure 15(c) is the mapping of NO_2 flux divergences. Positive values (red) indicate net emission zones, while negative values (blue) indicate net inflow regions. Maps were generated using QGIS Desktop 3.22.2 and Google Satellite Basemap. The flux divergence analysis over Singapore Figure 15(a) NO_2 concentrations derived from TROPOMI dataset (October–January 2018–2022) over Malaysia and Singapore reveals a strong smearing effect in the NO_2 concentration map, with elevated levels extending northward into Malaysia. However, the flux divergence map clearly localizes the emission source within Singapore, particularly in areas with dense industrial activity and power generation. This finding aligns with the Global Power Plant Database and EDGAR.

ISSN: 1686-6576 (Printed) | ISSN 2673-0014 (Online) | © Geoinformatics International

A similar pattern is observed in Kuala Lumpur and its surrounding region. While the NO_2 concentration map shows widespread elevated levels, the flux divergence map localizes the power plants and industrial activities located to the west of the city, particularly around Port Klang, Malaysia's largest and busiest port. The analysis shows a contrary result in Kuala Lumpur. This could be attributed to the higher influx of NO_2 pollutants from industrial activities in the western region compared to the relatively lower emissions from transportation reported by EDGAR in Kuala Lumpur, as well as the sinking or stopping of NO_2 transportation in this area.

4.2.5 Inland hotspots and supplementary analyses

Additionally, we present the analysis for inland hotspots in the Supplementary Information. The NO_2 concentrations over the areas, including Ho Chi Minh City, the largest city in Vietnam, Phnom Penh City and the nearby industrial area in Cambodia, Yangon City, a power plant near Mandalay in Myanmar, and the Mae Moh power plant in northern Thailand, are less affected by wind smearing. The flux divergence maps show typically ellipsoidal emission patterns cantered on the sources, indicating relatively calm wind conditions and more localized dispersion. These patterns confirm the effectiveness of the flux divergence method in identifying both point and area sources

5. Conclusion

This study provides a comprehensive analysis of the spatial and temporal characteristics of atmospheric NO_2 concentrations across Southeast Asia based on 18 years of OMI observations. The results demonstrate that elevated NO_2 concentrations are predominantly associated with major urban centers, where transportation-related emissions play a dominant role. The highest concentrations are observed over Singapore and Bangkok, followed by Hanoi and Kuala Lumpur, reflecting the intensity of urbanization and traffic-related activities in these cities.

Trend analysis reveals significant declines in atmospheric NO_2 concentrations over Bangkok, Haiphong, Kuala Lumpur, and most notably Singapore during the COVID-19 pandemic in early 2020, coinciding with widespread reductions in human activity, particularly transportation. These findings underscore the significant contribution of vehicular emissions to urban NO_2 pollution. In addition to urban sources, industrial activities contribute significantly to regional NO_2 levels. The Mae Moh power plant in Thailand and the northern industrial zone near Hanoi (specifically Haiphong city) rank as the third and fourth highest NO_2 hotspots in Southeast Asia. Trend analysis further indicates that NO_2 concentrations in the northern Vietnamese industrial zone have increased at the fastest rate in the region, reflecting the country's economic growth, especially in the industrial sector. Moreover, the combined analysis of long-term trends and seasonal variations provides a valuable framework for future monitoring and evaluation of air quality mitigation policies.

In addition to anthropogenic sources, the study also identifies biomass burning as a critical source of NO_2 pollution in Southeast Asia. Seasonal forest fires, recurring primarily between January and April, have a large-scale impact on regional air quality. Correlations between satellite-derived NO_2 concentrations and fire activity detected by the MODIS burned area product demonstrate the utility of satellite observations in monitoring pollution from biomass burning events. Quantitative analysis using linear regression for selected regions shows that an increase in burned area of 500x500 m^2 corresponds to average increases in atmospheric NO_2 concentrations of approximately 4.0974×10^{11} and 3.4830×10^{11} molecules/cm^2 in the Cambodia and Myanmar regions, respectively. These findings highlight the potential of satellite-derived NO_2 data to estimate emissions from biomass burning. Future global scale studies integrating satellite pollution datasets with fire activity databases could further refine such estimates by accounting for variations in forest types, combustion conditions, and regional environmental factors.

High-resolution TROPOMI observations, combined with flux divergence analysis, further enable detailed investigation of spatial NO_2 emission patterns across Southeast Asia. This study proves effective in mitigating the wind-induced smearing effect, which is particularly pronounced in coastal urban areas. While previous studies have demonstrated the utility of flux divergence in identifying point-source emissions, this study extends its application to more complex emission geometries. For instance, analysis of Bangkok reveals elevated flux divergence values concentrated along the city's perimeter, aligning with known emission zones.

Finally, this study also reveals a relationship between NO_2 dispersion patterns and regional topography. In the northern industrial zone in Vietnam, elevated NO_2 concentrations persist across a plateau bounded by surrounding terrain, with flux divergence indicating emission sources located primarily along the coastal edge. The spatial distribution of NO_2 closely follows the plateau's topographic boundaries, suggesting that transported atmospheric NO_2 is constrained by surrounding

ISSN: 1686-6576 (Printed) | ISSN 2673-0014 (Online) |

terrain, resulting in a spatial extent of elevated concentrations that closely matches the plateau area. A similar phenomenon is observed in Cambodia, where NO_2 concentrations associated with seasonal forest fires remain sharply confined near the Cambodia–Thailand border, coinciding with a sudden increase in terrain elevation. NO_2 originating from fires in Cambodia does not appear to cross this topographic boundary, indicating that atmospheric NO_2 in this region is largely confined below approximately 300 meters in altitude. Together, these findings demonstrate that regional topography plays an important role in modulating the horizontal and vertical dispersion of NO_2 in the lower atmosphere. Future studies could focus on regions worldwide where atmospheric NO_2 distributions correlate with topography may further enhance understanding of pollutant transport processes at regional and global scales.

References

[1] Air Quality Guidelines: Global Update 2005: Particulate Matter, Ozone, Nitrogen Dioxide, and Sulfur 1042 Dioxide. [online]. *World Health Organization*. Available: https://www.who.int/publications/i/item/WHO-SDE-PHE-OEH-06.02 [Access: Nov. 11, 2025].

[2] Hamra, G., Laden, F., Cohen, A. J., Raaschou-Nielsen, O., Brauer, M. and Loomis, D., (2015). Lung Cancer and Exposure to Nitrogen Dioxide and Traffic: A Systematic Review and Meta-Analysis. *Environmental Health Perspectives*. Vol. 123(11); 1107-1112. https://doi.org/10.1289/ehp.1408882.

[3] Crouse, D. L., Peters, P. A., Villeneuve, P. J., Proux, M. O., Shin, H. H., Goldberg, M. S., Johnson, M., Wheeler, A. J., W. Allen, R., Atari, D. O., Jerrett, M., Brauer, M., Brook, J. R., Cakmak S. and Burnett, R. T., (2015). Within- and Between-City Contrasts in Nitrogen Dioxide and Mortality in 10 Canadian Cities; A Subset of the Canadian Census Health and Environment Cohort (CanCHEC). *Journal of Exposure Science & Environmental Epidemiology*, Vol. 25(5); 482-489. https://doi.org/10.1038/jes.2014.89.

[4] Seinfeld, J. H. and Pandis, S. N., (2016). *Atmospheric Chemistry and Physics: From Air Pollution to Climate Change*. John Wiley & Sons, Hoboken.

[5] Bauwens, M., Compernolle, S., Stavrakou, T., Müller, J. F., vanGent, J., Eskes, H., Levelt, P. F., van der A, R., Veefkind, J. P., Vlietinck, J., Yu, H. and Zehner, C., (2020). Impact of Coronavirus Outbreak on NO_2 Pollution Assessed Using TROPOMI and OMI Observations. *Geophysical Research Letters*, Vol. 47(11). https://doi.org/10.1029/2020GL087978.

[6] Ambient (outdoor) Air Pollution. [Online]. *World Health Organization*. Available: https://www.who.int/news-room/fact-sheets/detail/ambient-(outdoor)-air-quality-and-health. [Accessed Jan. 24, 2024].

[7] Streets, D. G., Yarber, K. F., Woo, J. H. and Carmichael, G. R., (2003). Biomass Burning in Asia: Annual and Seasonal Estimates and Atmospheric Emissions. *Global Biogeochemical Cycles*, Vol. 17(4). https://doi.org/10.1029/2003GB002040.

[8] Goldberg, D., Anenberg, S., Lu, Z., Streets, D., Lamsal, L., McDuffie E. and Smith, S., (2021). Urban NO_x Emissions Around the World Declined Faster Than Anticipated between 2005 and 2019. *Environmental Research Letters*. Vol. 16(11). https://doi.org/10.1088/1748-9326/ac2c34.

[9] de Foy, B., Lu Z. and Streets, D., (2016) Satellite NO_2 Retrievals Suggest China Has Exceeded Its No_x Reduction Goals from the Twelfth Five-Year Plan. *Scientific Reports*. Vol. 6(1). https://doi.org/10.1038/srep35912.

[10] Tong, D. Q., Lamsal, L., Pan, L., Ding, C., Kim, H., Lee, P., Chai, T., Pickering K. E. and Ivanka, S., (2015). Long-term NO_x Trends over Large Cities in the United States During the Great Recession: Comparison of Satellite Retrievals, Ground Observations, and Emission Inventories. *Atmospheric Environment*. Vol. 107; 70-84. https://doi.org/10.1016/j.atmosenv.2015.01.035.

[11] Lamsal, L., Duncan, B., Yoshida, Y., Krotkov, N., Pickering, K., Streets D. and Lu, Z., (2015). U.S. NO_2 trends (2005–2013): EPA Air Quality System (AQS) Data Versus Improved Observations from the Ozone Monitoring Instrument (OMI). *Atmospheric Environment*, Vol. 110(2015); 130-143. https://doi.org/10.1016/j.atmosenv.2015.03.055.

[12] Curier, L., Kranenburg, R., Segers, A. J., Timmermans R. and Schaap, M. (2014) Synergistic Use of OMI NO_2 Tropospheric Columns and LOTOS–EUROS to Evaluate the Nox Emission Trends across Europe. *Remote Sensing of Environment*. Vol. 149(8); 58-69. https://doi.org/10.1016/j.rse.2014.03.032.

[13] Russell, A., Valin, L. and Cohen, R. C. (2012). Trends in OMI NO_2 Observations over the United States: Effects of Emission Control Technology 1066 and the Economic Recession. *Atmospheric Chemistry and Physics*. Vol. 12(24); 12197-12209. [online]. Available: https://acp.copernicus.org/articles/12/12197/2012/acp-12-12197-2012.pdf. [Access: May. 20, 2025].

[14] Xia, Y., Zhao Y. and Nielsen, C. P., (2016). Benefits of China's Efforts in Gaseous Pollutant Control Indicated by the Bottom-Up Emissions and Satellite Observations 2000–2014. *Atmospheric Environment*. Vol. 136; 43-53. https://doi.org/10.1016/j.atmosenv.2016.04.013.

[15] de Foy, B., Lu, Z. and Streets, D. G., (2016). Impacts of Control Strategies, the Great Recession and Weekday Variations on NO2 Columns above North American Cities. *Atmospheric Environment* Vol. 138; 74-86. https://doi.org/10.1016/j.atmosenv.2016.04.038.

[16] World Bank Country and Lending Groups. (2022). *World Bank.* Available: https://datahelpdesk.worldbank.org/knowledgebase/articles/906519-world-bank-country-and-lending-groups. [Accessed 15 July 2022].

[17] ASEAN Investment Report, (2022). *Pandemic Recovery and Investment Facilitation.* [online]. *ASEAN Secretariat*. Available: https://asean.org/wp-content/uploads/2022/10/AIR2022-Web-Online-Final-211022.pdf. [Accessed Jul. 24, 2024].

[18] Ambient Air Pollution: A Global Assessment of Exposure and Burden of Disease. (2016). *Clean Air Journal*, Vol. 26(2). [online]. Available: https://www.who.int/publications/i/item/9789241511353. [Accessed Jul. 24, 2024].

[19] Ambient Air Pollution Attributable Deaths, (2024). [Online]. *World Health Organization*. Available: https://www.who.int/data/gho/data/indicators/indicator-details/GHO/ambient-air-pollution-attributable-deaths. [Accessed Jul. 24, 2024].

[20] Reddington, C. L., Conibear, L., Robinson, S., Knote, C., Arnold S. R. and Spracklen, D. V., (2021). Air Pollution from Forest and Vegetation Fires in Southeast Asia Disproportionately Impacts the Poor. *GeoHealth,* Vol. 5(9). https://doi.org/10.1029/2021GH000418.

[21] Vadrevu, K. P., Lasko, K., Giglio, L., Schroeder, W., Biswas, S. and Justice, C., (2019). Trends in Vegetation Fires in South and Southeast Asian Countries. *Scientific Reports*, Vol. 9(1). https://doi.org/10.1038/s41598-019-43940-x.

[22] Blanford, H., (1958) Highlights of One Hundred Years of Forestry in Burma. *Empire Forestry Review*. Vol. 37(1); 33-42. [online]. Available: https://www.jstor.org/stable/42600438. [Accessed May 14, 2025].

[23] Grandstaff, T. B., (1980) Shifting Cultivation in Northern Thailand: Possibilities for Development, *United Nations University*, Tokyo [online]. Available: https://libcat.canterbury.ac.nz/Record/289277/Details?lng=ca [Accessed May 14, 2025].

[24] Inoue, Y., (2018). Ecosystem Carbon Stock, Atmosphere, and Food Security in Slash-and-Burn Land Use: A Geospatial Study in Mountainous Region of Laos. *In: Land-Atmospheric Research Applications in South and Southeast Asia.* 641-665. https://doi.org/10.1007/978-3-319-67474-2_28.

[25] Burrows, J. P., Weber, M., Buchwitz, M., Rozanov, V., Ladstatter-Weissenmayer, A., Richter, A., Debeek, R., Hoogen, R., Bramstedt, K., Eichmann, K. U. and Eisinger, M., (1999). The Global Ozone Monitoring Experiment (GOME): Mission Concept and First Scientific Results. *Journal of the 1086 Atmospheric Sciences*. Vol. 56(2); 151-175. https://doi.org/10.1175/1520-0469(1999)056<0151:TGOMEG>2.0.CO;2.

[26] Bovensmann, H., Burrows, J. P., Buchwitz, M., Frerick, J., Noël, S., Rozanov, V. V., Chance, K. V. and Goede, A. P. H., (1999). SCIAMACHY: Mission Objectives and Measurement Modes. *Journal of the Atmospheric Sciences,* Vol. 56(2); 127-150. https://doi.org/10.1175/1520-0469(1999)056<0127:SMOAMM>2.0.CO;2.

[27] Callies, J., Corpaccioli, E., Eisinger, M., Hahne, A. and Lefebvre, A., (2000). GOME-2-Metop's Second-Generation Sensor for Operational Ozone Monitoring. *ESA bulletin*. Vol. 102; 28-36. https://www.esa.int/esapub/bulletin/bullet102/Callies102.pdf.

[28] Jamali, S., Klingmyr, D. and Tagesson, T., (2020). Global-Scale Patterns and Trends in Tropospheric NO_2 Concentrations, 2005–2018. *Remote Sensing*, Vol. 12(21). https://doi.org/10.3390/rs12213526.

[29] van Geffen, J., Boersma, K. F., Eskes, H., Sneep, M., ter Linden, M., Zara, M. and Veefkind, J. P., (2020) S5P TROPOMI NO_2 Slant Column Retrieval: Method, Stability, Uncertainties and Comparisons with OMI. *Atmospheric Measurement Techniques,* Vol. 13(3); 1315-1335. https://doi.org/10.5194/amt-13-1315-2020.

[30] Schaap, M., Kranenburg, R., Curier, L., Jozwicka, M., Dammers, E. and Timmermans, R., (2013) Assessing the Sensitivity of the OMI-NO_2 Product to Emission Changes across Europe. *Remote Sensing*, Vol. 5(9); 4187-4208. https://doi.org/10.3390/rs5094187.

[31] Vadrevu, K. P., Lasko, K., Giglio, L., Schroeder, W., Biswas, S. and Justice, C., (2019). Quantification of Nitrogen Oxides Emissions from Build-Up of Pollution over Paris with TROPOMI. *Scientific Reports,* Vol. 9(1). https://doi.org/10.1038/s41598-019-56428-5.

[32] Bryan, C. A., (2022). *The Flux Divergence Method Applied to Nitrogen Emissions in the Netherlands*. Master's Thesis. TU Delft.

[33] Pseftogkas, A., Koukouli, M. E., Segers, A., Manders, A., Geffen, J., Balis, D., Meleti, C., Stavrakou, T. and Eskes, H., (2022). Comparison of S5P/TROPOMI Inferred NO_2 Surface Concentrations with in-situ Measurements over Central Europe. *Remote Sensing*, Vol. 14(19). https://doi.org/10.3390/rs14194886.

[34] Kim, D. R., Lee, J. B., Song, C. K., Kim, S. Y., Ma, Y. l., Lee, K. M., Cha, J. S. and Lee, S., (2015) Temporal and Spatial Distribution of Tropospheric NO_2 over Northeast Asia using OMI Data during the Years 2005–2010. *Atmospheric Pollution Research*. Vol. 6(5); 768-776. https://doi.org/10.5094/APR.2015.085.

[35] Han, K., (2019) Temporal Analysis of OMI-Observed Tropospheric NO_2 Columns over East Asia during 2006–2015. *Atmosphere*, Vol. 10(11). https://doi.org/10.3390/atmos10110658.

[36] Choi, Y., Kanaya, Y., Takashima, H., Irie, H., Park, K. and Chong, J., (2021) Long-Term Variation in the Tropospheric Nitrogen Dioxide Vertical Column Density over Korea and Japan from the MAX-DOAS Network, 2007–2017. *Remote Sensing*, Vol. 13(10). https://doi.org/10.3390/rs13101937.

[37] de Foy, B. and Schauer, J. J., (2022). An Improved Understanding of No_x Emissions in South Asian Megacities using TROPOMI NO_2 Retrievals. *Environmental Research Letters*, Vol. 17(2). https://doi.org/10.1088/1748-9326/ac48b4.

[38] Hou, Y., Wang, L., Zhou, Y., Wang, S., Liu, W. and Zhu, J., (2019). Analysis of the Tropospheric Column Nitrogen Dioxide over China Based on Satellite Observations during 2008–2017. *Atmospheric Pollution Research*, Vol. 10(2); 651-655. https://doi.org/10.1016/j.apr.2018.11.003.

[39] Wang, C., Wang, T., Wang, P. and Rakitin, V., (2020). Comparison and Validation of TROPOMI and OMI NO_2 Observations over China. *Atmosphere*, Vol. 11(6). https://doi.org/10.3390/atmos11060636.

[40] Zhao, Z., Lu, Y., Zhan, Y., Cheng, Y., Yang, F., Brook, J. R. and He, K., (2023). Long-Term Spatiotemporal Variations in Surface NO_2 for Beijing Reconstructed from Surface Data and Satellite Retrievals. *Science of The Total Environment*, Vol. 904. https://doi.org/10.1016/j.scitotenv.2023.166693.

[41] Levelt, P., Oord, G. H., Dobber, M., Malkki, A., Visser, H., Vries, J., Stammes, P., Lundell, J. and Sarri, H., (2006). The Ozone Monitoring Instrument. *IEEE Transactions on Geoscience and Remote Sensing,* Vol. 44(5); 1093-1101. https://doi.org/10.1109/TGRS.2006.872333.

[42] Boersma, K. F., Eskes, H. J., Dirksen, R. J., van der A, R. J., Veefkind, J. P., Stammes, P., Huijnen, V., Kleipool, Q. L., Sneep, M., Claas, J., Leitão, J., Richter, A., Zhou, Y. and Brunner, D., (2011). An Improved Tropospheric NO_2 Column Retrieval Algorithm for the Ozone Monitoring Instrument. *Atmospheric Measurement Techniques*, Vol. 4(9); 1905-1928. https://doi.org/10.5194/amt-4-1905-2011.

[43] Bucsela, E. J., Krotkov, N. A., Celarier, E. A., Lamsal, L. N., Swartz, W. H., Bhartia, P. K., Boersma, K. F., Veefkind, J. P., Gleason, J. F. and Pickering, K. E., (2013). A New Stratospheric and Tropospheric NO_2 Retrieval Algorithm for Nadir-Viewing Satellite Instruments: Applications to OMI. *Atmospheric Measurement Techniques*, Vol. 6(10); 2607-2626. https://doi.org/10.5194/amt-6-2607-2013

[44] Lamsal, L. N., Krotkov, N. A., Vasilkov, A., Marchenko, S., Qin, W., Yang, E. S., Fasnacht, Z., Joiner, J., Choi, S., Haffner, D., Swartz, W. H., Fisher, B. and Bucsela, E., (2021). Ozone Monitoring Instrument (OMI) Aura Nitrogen Dioxide Standard Product Version 4.0 with Improved Surface and Cloud Treatments. *Atmospheric Measurement Techniques,* Vol. 14(1); 455-479. https://doi.org/10.5194/amt-14-455-2021.

[45] van Geffen, J., Boersma, K. F., Eskes, H., Sneep, M., Ter Linden, M., Zara, M. and Veefkind, J. P., (2020). S5P TROPOMI NO_2 Slant Column Retrieval: Method, Stability, Uncertainties and Comparisons with OMI. *Atmospheric Measurement Techniques*. Vol. 13(3); 1315-1335. https://doi.org/10.5194/amt-13-1315-2020.

[46] Veefkind, J., Aben, I., McMullan, K., Förster, H., de Vries, J., Otter, G., Claas, J., Eskes, H., de Haan, J. K. Q., van Weele, M., Hasekamp, O., Hoogeveen, R., Landgraf, J., Snel, R., Tol, P., Ingmann, P., Voors, R., Kruizinga, B. and Vink, R., (2012). TROPOMI on the ESA Sentinel-5 Precursor: A GMES Mission For Global Observations of the Atmospheric Composition for Climate, Air Quality and Ozone Layer Applications. *Remote Sensing of Environment,* Vol. 120; 70-83. https://doi.org/10.1016/j.rse.2011.09.027.

[47] Giglio, L., Humber, M., Hall, J. V., Argueta, F., Boschetti, L. and Roy, D., (2022) *Collection 6.1 MODIS Burned Area Product User's Guide*. National Aeronautics and Space Administration [online]. Available: https://lpdaac.usgs.gov/documents/1006/MCD64_User_Guide_V61.pdf [Accessed Feb. 3, 2025].

[48] Giglio, L., Boschetti, L., Roy, D., Humber, M. and Justice, O., (2018). The Collection 6 MODIS Burned Area Mapping Algorithm and Product. *Remote Sensing of Environment*, Vol. 217(7); 72-85. https://doi.org/10.1016/j.rse.2018.08.005.

[49] ERA5 Hourly Data on Single Levels From 1940 to Present. (2025). [Online]. *European Centre for Medium-Range Weather Forecasts*. Available: https://cds.climate.copernicus.eu/datasets/reanalysis-era5-single-levels?tab=overview. [Accessed Feb. 3, 2025].

[50] Andrews, D., (2010). *An Introduction to Atmospheric Physics*. Cambridge University Press, Cambridge.

[51] Beirle, S., Borger, C., Dörner, S., Li, A., Hu, Z., Liu, F., Wang, Y. and Wagner, T., (2019). Pinpointing Nitrogen Oxide Emissions from Space. *Science Advances,* Vol. 15(11). https://doi.org/10.1126/sciadv.aax9800.

[52] Beirle, S., Borger, C., Dorner, S., Eskes, H., Kumar, V., de Laat, A. and Wagner, T., (2021). Catalog of NO_x Emissions from Point Sources as Derived from the Divergence of the NO_2 Flux for TROPOMI. *Earth System Science Data*, Vol. 13(6); 2995-3012. https://doi.org/10.5194/essd-13-2995-2021.

[53] Beirle, S., Boersma, K. F., Platt, U., Lawrence, M. G. and Wagner, T., (2011). Megacity Emissions and Lifetimes of Nitrogen Oxides Probed from Space. *Science,* Vol. 333(3); 1737-1739. https://doi.org/10.1126/science.1207824.

[54] Dix, B., Francoeur, C., Li, M., McDonald, B., Serrano, R., Veefkind, P., Levelt, P. and de Gouw, J., (2021). *No_x Emissions from U.S. Oil and Gas Production using TROPOMI NO_2 and The Divergence Method*. EGU General Assembly Conference. [online]. Available: https://ui.adsabs.harvard.edu/abs/2021EGUGA.2313554D/abstract [Access: Aug. 20, 2025]

[55] Romahn, F., Pedergnana, M., Loyola, D., Apituley, A., Sneep, M. and Veefkind, J., (2022) *Sentinel-5 precursor/TROPOMI Level 2 Product User Manual Formaldehyde HCHO*. Royal Netherlands Meteorological Institute [Online]. Available: https://sentiwiki.copernicus.eu/__attachments/1673595/S5P-L2-DLR-PUM-400F%20-%20Sentinel-5P%20Level%202%20Product%20User%20Manual%20Formaldehyde%20HCHO%202022%20-%202.4.pdf?inst-v=87ef0ca0-8091-4ed6-bc9f-05ea3a6bc632. [Access: Aug. 20, 2025]

[56] Byers, L., Friedrich, J., Hennig, R., Kressig, A. Li, X., Valeri L. and McCormick, C., (2018) *A Global Database of Power Plants*. World Resources Institute. [Online]. Available: https://www.wri.org/research/global-database-power-plants [Access: Aug. 20, 2025]

[57] Crippa, M., Guizzardi, D., Muntean, M., Schaaf, E., Dentener, F., van Aardenne, J. A., Monni, S., Doering, U., Olivier, J. G. J., Pagliari, V. and Janssens-Maenhout, G. (2018) *Global Air Pollutant Emissions - EDGAR v5.0* European Commission. [Online]. Available: https://edgar.jrc.ec.europa.eu/dataset_ap50 [Access: Aug. 20, 2025].

[58] Lehner, B. and Grill, G., (2013) Global River Hydrography and Network Routing: Baseline Data and New Approaches to Study the World's Large River Systems. *Hydrological Processes*, Vol. 27(15); 2171-2186. https://doi.org/10.1002/ hyp.9740.